Title: In vivo spatiotemporal patterns of oligodendrocyte and myelin damage at the neural electrode interface.

Keying Chen [a, b], Steven M. Wellman [a, b], Yalikun Yaxiaer [c], James R. Eles [a, b], Takashi DY. Kozai [a, ,b, d, e, f, *]
[a] Department of Bioengineering, University of Pittsburgh, USA
[b] Center for the Neural Basis of Cognition, University of Pittsburgh and Carnegie Mellon University, USA
[c] Eberly College of Science, Pennsylvania State University, University Park, USA
[d] Center for Neuroscience, University of Pittsburgh, USA
[e] McGowan Institute of Regenerative Medicine, University of Pittsburgh, USA
[f] NeuroTech Center, University of Pittsburgh Brain Institute, USA

* Corresponding author: tk.kozai@pitt.edu

Abstract:
Intracortical microelectrodes with the ability to detect intrinsic electrical signals and/or deliver electrical stimulation into local brain regions have been a powerful tool to understand brain circuitry and for therapeutic applications to neurological disorders. However, the chronic stability and sensitivity of these intracortical microelectrodes are challenged by overwhelming biological responses, including severe neuronal loss and thick glial encapsulation. Unlike microglia and astrocytes whose activity have been extensively examined, oligodendrocytes and their myelin processes remain poorly studied within the neural interface field. Oligodendrocytes have been widely recognized to modulate electrical signal conductance along axons through insulating myelin segments. Emerging evidence offers an alternative perspective on neuron-oligodendrocyte coupling where oligodendrocytes provide metabolic and neurotrophic support to neurons through cytoplasmic myelin channels and monocarboxylate transporters. This study uses *in vivo* multi-photon microscopy to gain insights into the dynamics of oligodendrocyte soma and myelin processes in response to chronic device implantation injury over 4 weeks. We observe that implantation induces acute oligodendrocyte injury including initial deformation and substantial myelinosome formation, an early sign of myelin injury. Over chronic implantation periods, myelin and oligodendrocyte soma suffer severe degeneration proximal to the interface. Interestingly, wound healing attempts such as oligodendrogenesis are initiated over time, however they are hampered by continued degeneration near the implant. Nevertheless, this detailed characterization of oligodendrocyte spatiotemporal dynamics during microelectrode-induced inflammation may provide insights for novel intervention targets to facilitate oligodendrogenesis, enhance the integration of neural-electrode interfaces, and improve long-term functional performance.

Keywords: Brain-computer interface; neurotechnology; foreign body response; biocompatibility; bio-integration; neural interfaces

Introduction
Brain implantable microelectrodes are advanced tools that capture bioelectrical signals *in vivo* and deliver electrical pulses to local brain areas [1, 2]. These microelectrodes have great potential in exploring mechanisms underlying neurological disorders such as Alzheimer's disease [3, 4], multiple sclerosis [5], Parkinson's disease [6-8], stroke [9-11], etc. In addition, they show great promise in restoring sensory perception and/or functional motor control for disabled patients [1, 12, 13]. To further improve the potential of these invasive intracortical microelectrodes, it is necessary to preserve the integrity of the tissue-electrode interface over chronic implantation periods. This helps maintain reliable high-amplitude neural recordings from healthy, normal-functioning neurons in close proximity to the microelectrode [14-16]. However, current limitations in biocompatibility lead to a decline in long-term functional performance, making it challenging to interpret recorded neural signals over long time periods and hinders the application of these devices [17-19]. Many novel microelectrode designs aim to optimize single parameters such as size [20, 21], geometry [22, 23], softness [23-25], material [26, 27], chemical surface modifications [28], and packaging [29] in order to minimize local neuroinflammation and improve the efficacy of chronically implanted microelectrodes. However, functional recording performance and the degree of tissue reaction heavily rely on interdependent interactions between distinct physical properties of the device and different neuronal and non-neuronal cell types within the brain [17, 23]. Although novel microelectrode designs provide promising directions for the next generation of bioelectronic interfaces, traditional silicon-based intracortical microelectrodes remain one of the most used brain technologies. Revealing previously unexplored biological mechanisms behind long-term failure of functional intracortical microelectrodes can provide insights on novel strategies to seamlessly integrate brain tissue with microelectrodes.

Implantation of intracortical microelectrodes triggers a series of biological inflammatory cascades that disturbs the local tissue microenvironment surrounding the probe surface [30, 31], an area which corresponds to where most electrophysiological signals are collected [32-34]. The insertion of a stiff silicon probe inevitably ruptures the blood brain barrier (BBB), leading to infiltration of blood cells and plasma protein into the brain tissue [31, 35, 36]. Microglia respond immediately to these inflammatory proteins as well as the inserted probe by polarizing processes toward the microelectrode within the first few minutes after implantation beforemigrating to the probe surface over hours to days [37]. Astrocytes also become activated with hypertrophic morphology, migrating, and forming a layer of encapsulating scar alongside with microglia [38]. Following implantation, there is a gradual loss of neurons near the electrode due to oxidative stress [22], metabolic stress [35], and a high expression of pro-inflammatory cytokines [37, 39] and extracellular glutamate [40]. It has been widely accepted that microglia and astrocytes are two major glia that participate in insertion-induced neuroinflammation and glial scarring. Together, they contribute to the impairment of neuronal integrity and ultimately result in the decline in functional recording performances. However, recent immunohistochemical data revealed discrepancies between minimal microglia and astrocyte activation around the implant and poor electrophysiological performance, indicating additional cellular players may be involved in neuroinflammation and the decline of functional recording performances [35]. These findings suggest that the limitation of current therapeutic interventions may be due to misplaced emphasis on microglia and/or astrocyte activation.

Oligodendrocytes maintain neuronal homeostasis through direct neurite contact with myelin sheaths [41].Oligodendrocyte precursor cells (OPCs) act as a multi-potent reservoir for oligodendrocytes, astrocytes, and even neurons in response to distinct signaling [31, 42, 43] and are highly involved in neuroinflammation at the neural-electrode interface [30]. Growing evidence supports the idea that these understudied glia, oligodendrocytes, their myelin processes, and oligodendrocyte precursor cells, are key factors in chronic neurodegenerative diseases [41, 44-46]. These findings suggest that chronic failure of intracortical microelectrodes may arise from dysfunction of overlooked cell types which, in turn, negatively influence long-term neuronal functionality. While we have previously demonstrated that oligodendrocytes are necessary for functional recording performance [47], the spatiotemporal dynamics of how oligodendrocytes and myelin react to intracortical microelectrode implantation injury are still unknown. Filling this gap in knowledge is crucial for developing a comprehensive understanding of the biological reactions occurring at the microelectrode interface and elucidating appropriate targets and timing for key interventions.

Compared to other glia within the CNS, oligodendrocytes have more direct interaction with neuronal integrity and functionality through large myelin-axon contact areas. A single oligodendrocyte can generate myelin sheaths over multiple neuronal axons [48], allowing a wide coverage of lipid-rich myelination. It is commonly acknowledged that the role of oligodendrocytes is to produce myelin sheaths for passive insulation around axons and modulate conduction velocity of action potentials, enhancing the activity of the neural network. This may account for high myelination density in white matter tracks; however, oligodendrocytes and myelin are also present within the cortical grey matter [41, 48]. In addition to supporting conduction velocity, oligodendrocytes provide important metabolic support to nearby neurons [41, 48]. Neurons experience a heavy metabolic burden following electrical activity over long, distal axonal projections while possessing limited energy storage capacity, which renders them highly vulnerable to inflammation during brain injury and disease [49, 50]. More recent evidence has shown that oligodendrocytes provide neurotrophic and metabolic support to neurons during neuronal and astrocytic signaling [51-53]. This is especially important considering neurons are incapable of storing glucose as glycogen [54, 55]; instead they rely on oligodendrocytes as well as astrocytes to provide supplemental energy during hypoxic conditions [56]. Oligodendrocytes can provide energy substrates, either produced intracellularly or transported to oligodendrocytes from astrocytes via gap junctions, to local axons within myelin internodes via monocarboxylate transporters (MCTs) [51, 57, 58]. Knockout models indicate that mutations in oligodendrocyte specific proteins cause severe axonal degeneration independent of electrical conductance [59-61], implying the metabolic support provided by oligodendrocytes is essential for energy homeostasis in neurons. Using whisker stimulation, Hughes et al. showed that oligodendrocytes and myelin maintain strong correlation with the activity levels of neuronal circuits within the cortex [62], reflecting the coincidence of oligodendrocyte and myelin dynamics alongside neuronal energy demands. Therefore, revealing the fate of oligodendrocytes and myelin around the implant site is important for understanding neuronal health and activity near implanted intracortical microelectrodes.

Oligodendrocytes and myelin function to facilitate signal transduction to axonal terminals as well as maintain local axonal energy balance and structural integrity, which are susceptible targets in neurodegenerative diseases and brain injury [45, 49, 63]. For example, multiple sclerosis (MS) is a well-studied neurodegenerative disease characterized as continuous damage exclusive to oligodendrocytes. The progression of MS results in demyelination and ultimately axonal death,

leading to paralysis and cognitive decline. This suggests that oligodendrocytes support functional myelin-axon coupling and affect neuronal survival [64, 65]. Additionally, studies of ischemic stroke and traumatic brain injury suggest that oligodendrocytes and myelin structures are highly susceptible to inflammatory environments including oxidative stress, metabolic deprivation, and glutamate-induced excitotoxicity that can occur at the injury site, which correlates with severe neuronal network dysfunction and behavioral outcomes [66]. Furthermore, we previously showed that global depletion of cortical oligodendrocytes can severely impair the quality of recorded electrophysiological signals [47]. Interestingly, at chronic timepoints, when oligodendrocytes within the microenvironment around the implant have degenerated, electrophysiological signals declined to match the oligodendrocyte-depleted tissue despite having similar neuronal densities [47]. This indicates that oligodendrocytes play a role in electrophysiological recording performance. Overall, these studies demonstrate the importance of oligodendrocytes and myelin in neuronal health and highlight their potential as a novel therapeutic target to mitigate neuronal degeneration around intracortical microelectrode interfaces. However, the spatiotemporal dynamics of oligodendrocytes and myelin to intracortical microelectrode implantation have yet to be understood.

Therefore, the goal of this study aims to answer when, where, and how oligodendrocytes and myelin respond to the implanted microelectrode over a chronic 4-week implantation period and provide a real-time spatiotemporal characterization for the design of future therapies and interventions. Understanding how oligodendrocytes and myelin are injured at the electrode-tissue interface will provide novel perspectives on biological mechanisms underlying chronic device performance failure and help identify novel strategies for improving tissue health and chronic device capabilities. Here, we apply multi-photon microscopy in transgenic mice expressing fluorescent labels in oligodendrocytes and myelin to characterize their integrity and health around chronically implanted microelectrodes *in vivo*, allowing dynamic visualization of cellular activity at the electrode-tissue interface. We observed that oligodendrocytes and myelin undergo morphological distortion during initial device insertion prior to the onset of myelin injury and the of myelin-associated protrusions, called myelinosomes, with increasing accumulation at the device-tissue interface. We also observed patterns of oligodendrocyte and myelin degeneration within the device interface region. Overall, implantation of intracortical microelectrodes disrupts the integrity of myelin sheaths and leads to progressive degeneration of myelinating lineage structures. However, oligodendrocytes also demonstrate an intrinsic property to regenerate and remyelinate, suggesting that these cells have the potential to improve neuronal health and functional performance of implanted intracortical microelectrodes over time.

2. Method

2.1 Surgical probe implantation

Transgenic mice expressing green fluorescent protein under the *Cnp* promoter (male, 25-30 g, n = 5, Tg(Cnp-EGFP*)1Qrlu/J, Jackson Laboratories; Bar Harbor, ME) were used to track oligodendrocytes and myelin dynamics. Four-shank 16-channel Michigan-style non-functional silicon microelectrodes (A4x4-3mm-100–703-CM16; NeuroNexus, Ann Arbor, MI) were used for implantation. Two-photon implantation surgery and chronic window installation were performed as previously published [31, 37, 40, 67]. Prior to surgery, animals were sedated using an intraperitoneal (IP) injection of 75 mg/kg ketamine and 7 mg/kg xylazine. Then, mice were head-fixed in a stereotaxic frame and administered oxygen. A heating pad was used to maintain body temperature. An initial incision was performed to remove skin and connective tissue from the bone prior to applying Vetbond (3M, Saint Paul, MN) to the skull surface. Two holes were drilled with a high-speed dental drill over both motor cortices for bone screw insertion. Bilateral craniotomies at a 3 mm by 3 mm dimension were drilled over the visual cortex (1.5 mm anterior to lambda and 1 mm lateral from the midline) on two hemispheres. During drilling, saline was periodically administrated over the skull surface to avoid thermal damage. Microelectrode shanks were implanted at a 30° angle with an oil-hydraulic microdrive (MO-81, Naishige, Japan, 200 μm/s) while avoiding large blood vessels visible on the brain surface. Microelectrodes were inserted 600 μm into the cortex up to a resting depth of 250 – 300 μm below the pial surface (Layer II/III). For sealing, Kwik-sil (World Precision Instruments, Sarasota County, FL) was filled into the craniotomy and secured with a glass coverslip followed by dental cement. Finally, a dental cement well was built at the edge of both craniotomies to hold saline for imaging using a water-immersive objective lens. All procedures and experimental protocols were approved by the University of Pittsburgh, Division of Laboratory Animal Resources, and Institutional Animal Care and Use Committee in accordance with the standards for humane animal care as set by the Animal Welfare Act and the National Institutes of Health Guide for the Care and Use of Laboratory Animals.

2.2 Two photon imaging

Two-photon *in vivo* imaging was performed as published previously [31, 37, 40, 67]. Data collection was performed using a two-photon laser scanning microscopy system which includes a scan head (Ultima IV, Bruker, Madison, WI), an OPO laser (Insight DS+; Spectra-Physics, Menlo Park, CA) at a wavelength of 920 nm, non-descanned photomultiplier tubes (Hamamatsu Photonics KK, Hamamatsu, Shizuoka, Japan), and a 16x, 0.8 numerical aperture water immersion objective lens (Nikon Instruments, Melville, NY). Laser power was maintained at 20-40 mW during all imaging sessions to prevent thermal tissue damage. Light isoflurane (1.0–1.5%) was administrated to each animal prior to imaging. Then, animals were head-fixed within a stereotaxic frame and injected IP with sulforhodamine 101 (SR101) for vessel visualization. Z-stacks taken at a resolution of 1024 x 1024 pixels (407.5 × 407.5 μm in the x-y plane) every 2 μm along the microelectrode shanks were acquired in both ipsilateral and contralateral tissue. Frequency of imaging occurred at 1, 3, 6, 9, 12, 24, 48, and 72h after implantation and then daily until day 14 and then weekly up to 28 days post-implantation.

2.3 Data analysis

Z-stacks acquired from CNP-EGFP transgenic mice were examined for changes in oligodendrocyte and myelin sheath morphology. Since myelin is distributed within the x-y plane in superficial cortical layers (Layer I) and descends in the z-direction into deeper cortex, quantifications of myelin and oligodendrocyte morphologies were mainly in Layer I. In order to minimize noise interference, each z-stack was first processed in ImageJ with background subtraction (rolling ball radius = 10), 1-pixel 3D median filter, and de-speckle prior to morphological assessment.

2.3.1 Analysis of myelin distribution and oligodendrocyte shape

Myelin distribution was quantified as the orientation angle of individual myelin sheaths using a customized MATLAB program. A previous study suggests that the mechanical strain on the surrounding brain tissue is mainly concentrated within the first 25 μm from the electrode surface [68]. Therefore, regions of interest (ROIs) at the electrode-tissue interface were chosen as a 75 μm x 25 μm rectangle adjacent to the outmost microelectrode shank, while ROIs in contralateral and distal tissue (> 250 μm) were selected at the same size. This quantification method of myelin distribution was previously described in [67]. Briefly, ROIs were processed with a morphological opening operation ('imopen' in MATLAB) to remove noise as well as preserve myelin shape. Then, a 25-pixel long linear structuring element of 11 different angles (15–180° in increment of 15°) was used for identifying the orientation of targeted myelin segments within the ROI. In order to avoid dual measurement (0° and 180°) within the horizontal direction, only 180° was included in the linear structuring element. Each pixel above Otsu's intensity thresholding reported the angle which had the highest morphological opening response in the linear structuring element. The orientation angles of myelin at interface, distal, and contralateral ROIs were plotted as histograms and statistically compared using a Kolmogorov-Smirnov test (significance: $p < 0.05$).

Oligodendrocyte cell somas have a circular shape with diameters ranging from 10-20 μm under normal conditions. These cells were manually outlined and morphologically fitted in ImageJ. Taking into consideration the range of diameters and sparse distribution of oligodendrocytes, ROIs within the interface for quantifying oligodendrocyte cell shape strain index (CSSI) and cell elongation angle (CEA) were increased to 75 μm x 50 μm. The calculation methods for fitting deformed elliptical oligodendrocytes with major (b) and minor (a) axes are described in previous publications [67, 69]. CSSI was calculated as extent of mechanical strain (ΔL) over the mean diameter of the cell body without strain (L_0) to describe the level of shape deformation in Eq. (1):

$$CSSI = \frac{\Delta L}{L_0} = \frac{(b-a)}{\frac{(b+a)}{2}} \quad (1)$$

Greater CSSI values imply a more elliptic, strained cell body while smaller CSSI values represent a relatively circular soma without strain. The mean CSSI was statistically compared with one-way ANOVA followed by Tukey post hoc. CEA was defined as the angle between the major axes and the radial line from the cell center perpendicular to the implant surface, implicating the strain direction of the cell body was altered from healthy conditions [69]. Oligodendrocytes in tissue over 50 μm away from the implant were also quantified for CEA as control. CEA of oligodendrocytes within 50 μm within interface and control ROIs (> 50 μm) were plotted in box plots and statistically evaluated with an unequal variance Welch's t-test (significance: $p < 0.001$).

2.3.2 Myelinosome tracking analysis

Following z-stack filtering in ImageJ, myelinosomes were identified as swollen, spherical protrusions ranging in diameter from 2-8 μm. Myelinosomes were counted and measured in diameter in 75 μm x 25 μm rectangular ROIs from the surface of the implant up to 250 μm away over 28 days as well as in contralateral ROIs for normalization. Myelinosomes near the electrode-tissue interface were normalized to contralateral ROIs and were binned every 25 μm horizontally from probe

surface to 250 μm away and statistically compared to the most distal bin (225-250 μm) using two-way ANOVA followed by Dunnett's post hoc. Changes in normalized myelinosome density at the interface over time were visualized by a restricted akima spline which goes through every data point with tighter turns. Two-way ANOVA followed by Dunnett's post hoc was performed to determine significant changes in normalized myelinosome densities compared to 28 days post-insertion. Overall spatiotemporal patterns in normalized myelinosome density were determined using linear regression with respect to distance away from the probe at each time point. Calculated regression slopes (Spatial Gradient) as well as y-intercepts (Proximal Density) were reported over time and statistically compared with other time points using one-way ANOVA followed by Tukey post hoc.

The diameter of a myelinosome is an important indicator of early myelin injury and dynamically changes over time. Therefore, variation in the diameter of myelinosomes near the implanted probe over time was quantified. To determine the effect of microelectrode implantation on myelinosome morphology, the diameter of myelinosomes at the electrode-tissue interface were normalized to the mean diameter of myelinosomes within contralateral ROIs. Normalized myelinosome diameters within the first 100 μm were plotted as a function of time up to 28 days post-insertion by a restricted akima spline. Two-way ANOVA followed by Bonferrroni-corrected t-tests were performed to test whether significance exists for normalized myelinosome diameter between consecutive time points. The relationship of normalized myelinosome diameter over time at each distinct spatial bin was measured using linear regression, which was statistically compared with an unequal-variance Welch's one-way ANOVA followed by Holm and Sidak's post hoc between each time point.

To track individual myelinosome development over time and investigate possible incidences of demyelination, myelinosomes (n = 36) were individually traced within 100 μm of the electrode-tissue interface over time until the point of degeneration. The length of myelin sheath associated with a myelinosome protrusion was measured at both the initial time point when the myelinosome was identified and end time point when the myelinosome eventually disappeared. Myelinosome degeneration was classified into two categories: following demyelination, indicated by length of myelin at the end point of myelinosome degeneration as less than the length compared to 1 hour post implantation, or morphologically intact, with myelin length being equal between those two time points. A paired Student's t-test was performed to determine significance between the two classified states (demyelination and morphologically intact).

2.3.3 Myelin density assessment

Since imaging parameters used to acquire z-stacks during two-photon imaging differ between time points, intensity-based analysis was not appropriate for myelin density quantification. Instead, myelin density was defined as the total length of manually identified myelin sheaths within interface ROIs, while the total myelin length within the contralateral side was used as control for normalization. The ROIs used for myelin density analysis were the same ROIs used for myelinosome density quantification. Normalized myelin density was measured as a function of distance from the surface of the implant and statistically compared by two-way ANOVA followed by Dunnett's post hoc where normalized myelin density at 1h post-insertion was used as the control. Changes in normalized myelin density with respect to time were modeled by fitting a nonlinear third order polynomial curve and statistically tested for group-wise significance between binned distances using likelihood ratio tests. 95% confident intervals for each nonlinear curve of normalized myelin density over distance and time were calculated and plotted. Similar to spatiotemporal myelinosome quantification, normalized myelin density was modeled by linear regression that reported regression slope (Myelin Spatial Gradient) as well as regression intercept (Proximal Myelin Density). These two metrics were plotted over time and statistically compared by two-way ANOVA with Tukey post hoc. In order to investigate temporal patterns between myelinosome formation and myelin density, normalized myelinosome and myelin density at a radius of 100 μm away from the implant were represented as a difference in percentage calculated by changes between two consecutive time points divided by the average value. Positive differences in percentage indicates an increase in myelinosome/myelin density at the current time point relative to previous one, while negative differences in percentage indicates a decrease in quantification metrics compared to the previous time point. An index of zero indicates no obvious changes between two consecutive time points. One-way ANOVA followed by Bonferroni corrected t-test comparisons were used to identify significant transitions in myelinosomes/myelin density over time.

In addition, the ratio of the number of myelinosomes over the total myelin length within an ROI can be an indicator for severity of myelin injury. The amount of myelinosomes and the total length of myelin processes used for ratio calculation shared the same ROIs in radial bins from the probe surface up to 250 μm away from the implant. The myelinosome/myelin ratio within contralateral ROIs for each time point was used as a normalization control. Changes in ratio of myelinosome density over myelin density in bins and at different time points were compared with two-way ANOVA followed by Dunnett's test with 225-250 μm distal bin and 28 days post-insertion as control, respectively. The

spatiotemporal patterns of myelinosome/myelin ratio was determined using linear regression as described above. Coefficients were reported as spatial gradient (slope) and proximal ratio (y-intercept) on distance distribution and statistically compared between consecutive time points using one-way ANOVA followed by Tukey post hoc.

2.3.4 Quantification of oligodendrocyte degeneration and regeneration

Oligodendrocytes were identified as solid, circular cell bodies with diameters of ~10-15 μm at each time point using ImageJ. First, z-stacks between consecutive time points were aligned to each other as described previously [31], and the spatial XY coordinates of oligodendrocytes on the implantation side were recorded with an ImageJ built-in feature "Measure". Oligodendrocytes were determined to be degenerated if the cell body that appeared in the same location in the previous timepoint was no longer present in the same location in subsequent z-stacks. Newly differentiated oligodendrocytes were defined as new soma that appeared at distinct XY coordinates within the current z-stack. Degenerated oligodendrocytes as well as newly-appeared oligodendrocytes were binned every 50 μm radially from the implant, and t-tests corrected using Holm-Sidak's method were performed to test the significance between degenerated and newly-appeared oligodendrocytes at each bin In order to investigate the temporal dynamics of oligodendrocyte density, the rate of change in overall oligodendrocyte density (percent/day) was calculated by the difference in oligodendrocyte populations between two consecutive time points (current time point: tp2; previous time point: tp1) divided by the total oligodendrocyte quantity from the previous time point (tp1), eq(2):

$$rate\ of\ changes\ in\ overall\ OL\ density\ (\%/day) = \left(\frac{\#OL_{tp2} - \#OL_{tp1}}{\#OL_{tp1}}\right) \div \Delta t \quad (2)$$

Meanwhile, the cumulative rate of change in oligodendrocyte density was defined as the total amount of specific oligodendrocyte population i between the current time point and 1h post-implantation divided by the total amount of oligodendrocytes at 1h post implantation, while i could denote either degenerated or newly-appeared oligodendrocytes:

$$cumulative\ percentage\ of\ changes\ in\ OL_i\ density\ (\%) = \frac{\#OL_{\boldsymbol{i}_{current\ tp}} - \#OL_{\boldsymbol{i}_{@1h}}}{\#OL_{\boldsymbol{i}_{@\ 1h}}} \quad (3)$$

$$i = degenerated, newly\ generated, perivascular, or\ non-perivascular$$

The temporal rates of change of oligodendrocyte density including rate of change in overall density, cumulative degeneration, and cumulative newly-appeared population within 250 μm from the probe were quantified and compared between consecutive time points with one-way ANOVA followed by Bonferroni-corrected t-tests.

The morphological subtype of oligodendrocytes that reside along blood vessels, called perivascular oligodendrocytes, were also characterized. Perivascular oligodendrocytes were identified and measured by the distance between the edge of their cell bodies and the wall of nearest blood vessels (edge-to-edge distance, μm) within the z-stack. The histogram of edge-to-edge distances was made using a bin size of 5 μm, where the minimal value of edge to edge distance was determined as 0 μm when the measurement was less than the minimum pixel resolution (0.4 μm/ pixel). Perivascular oligodendrocytes were defined as the oligodendrocytes < 0.4 μm/pixel edge-to-edge distance with the closet blood vessel and divided into three categories based on the surrounding vessel subtypes: capillaries, veins, and arteries. Then, in order to figure out the effect of implantation injury on perivascular oligodendrocytes, degenerated oligodendrocytes tracked over 28 days post-implantation relative to 1h control were separated based on the edge-to-edge distance to vasculature into two groups, perivascular and non-perivascular oligodendrocytes (paired t-test). In addition, the rate of change in perivascular and non-perivascular oligodendrocytes over 4 weeks at interface (< 250 μm) and distal (> 250 μm) ROIs was calculated in eq (3) and statistically compared with two-way ANOVA followed by Tukey post hoc (significance: $p < 0.05$).

3. Results

Lightly anesthetized CNP-EGFP transgenic mice were used to study the spatiotemporal dynamics of oligodendrocytes and myelin in response to silicon microelectrode implantation over a chronic 4-week period (Fig. 1A). Enhanced green fluorescent protein (EGFP) anchored within the membrane was genetically driven by the 2',3'-cyclic nucleotide 3' phosphodiesterase (*Cnp*) promoter [70], which enables visualization of brain oligodendroglia and myelin processes chronically through sealed craniotomy windows (Fig. 1B). This allowed myelinated fibers to be observed in Layer I-III using two-photon microscopy [62, 71]. Cortical Layer I contains a sufficient amount of oligodendrocytes and myelin [62]. Therefore, observations of oligodendrocytes and myelin dynamics around implanted microelectrodes using two-photon microscopy were focused on Layer I. Probes were implanted at a 30° angle into the visual cortex while avoiding penetration through large vasculature during insertion (Fig. 1C), as previously described [31, 67]. Regions of interest (ROIs) were defined within the first 250 μm adjacent to the outmost shank, whereas distal ROIs were defined as > 250 μm

away from the probe (Fig. 1D). A contralateral craniotomy window of the same dimension was also performed and used as control to normalize damage associated with the craniotomy. Thus, fluorescent responses within the cranial window reflects oligodendrocyte responses to implantation injury as well as the foreign body response associated with the device over 28 days in the visual cortex, since these two injury components cannot be decoupled via chronic electrophysiology. Z-stacks were acquired during each imaging session in each animal without surface bleeding or bone regrowth under the craniotomy window over the entire 4-week period. SR101 was intraperitoneally (IP) injected prior to each imaging session to visualize the vasculature, which provided landmarks for oligodendrocyte and myelin due to subtle tissue volume variation that may occur during chronic implantation, such as tissue swelling and scar formation.

3.1. Oligodendrocytes and myelin processes suffer mechanical distortion during microelectrode implantation

The mismatch in mechanical properties between stiff silicon probes and soft, flexible brain tissue leads to mechanical strain in the tissue around the microelectrode implant. This strain can contribute to local neurodegeneration and the loss of functional device performances. To determine the extent of mechanical strain on oligodendrocytes and myelin processes at the tissue-electrode interface, strain-induced deformation of oligodendrocyte soma and myelin adjacent to the implant were compared to distal and contralateral tissue regions.

Morphological changes to myelin processes were quantified as the distribution of myelin angle with respect to the probe surface [67]. These linear myelin elements had angles ranging from 15^o – 180^o and were grouped in 15^o intervals. At 1h immediately after microelectrode implantation, myelin processes near the interface were aligned parallel with the implant, while myelin processes in distal and contralateral ROIs were aligned in random directions (Fig. 2A). The Kolmogorov-Smirnov test demonstrated statistical group-wise significance in myelin angle distribution between interface and distal (> 250 μm) areas ($p < 0.05$) and between interface and contralateral regions ($p < 0.05$; Fig. 2B), demonstrating that implantation altered local myelin orientation due to mechanical strain at the electrode-tissue interface. This observation was consistent with mechanical distortion in neuronal soma and neurites in response to the initial microelectrode implantation [67], which leads to abnormal calcium activity close to the implant and a sequential loss in integrity of neuronal compartments [72] and signal strength recorded by functional microelectrode devices [68].

The extent of strain-induced oligodendrocyte soma deformation was measured by two quantitative metrics, Cell Shape Strain Index (CSSI) and Cell Elongation Angle (CEA) (Fig. 2C). CSSI quantified the group-wise level differences in soma shape from a perfect circle, which measures the population effect of mechanical strain on oligodendrocytes after probe implantation. At 1h post-implantation, oligodendrocytes within 50 μm of the probe had CSSI values of 0.5299 ± 0.1509, which was significantly higher than CSSI of oligodendrocytes in distal and contralateral regions, 0.1843 ± 0.1121 and 0.1152 ± 0.1001, respectively (Fig. 2D; one-way ANOVA with Tukey post hoc, $p < 0.0001$). This suggests that implantation of microelectrodes in the brain deforms local oligodendrocyte somas into elliptic shapes.

To determine the orientation of this oligodendrocyte deformation, CEA was measured to describe the angle of the longer axis of the fitted ellipses on the soma relative to the radial line normal to the electrode shank. Higher CEA indicates that the mechanical strain on the soma is due to the strain profile generated by the accommodation of probe volume. Contralateral ROIs were excluded from the CEA analysis since contralateral regions do not have an implant. Due to the sparse distribution of oligodendrocytes in Layer I and the fact that mechanical force from an implanted probe was limited to the first 50 μm from the probe surface [35, 68], CEA controls were chosen as oligodendrocytes >50 μm away the implant surface and had an angle of $53.59^o \pm 19.43^o$. These oligodendrocytes were significantly different from oligodendrocytes within the first 50 μm, which had an angle of $74.00^o \pm 8.775^o$ (Fig. 2E; unequal variance Welch's t-test, $p < 0.0001$). This result implies that deformation of oligodendrocytes occurs along the direction parallel to shear strain introduced by the implanted microelectrode. As a result, oligodendrocyte morphology and myelin distribution undergo changes in alignment within the electrode-tissue interface following device implantation.

3.2. Dynamic patterns of myelinosomes are indicative of early myelin injury following microelectrode implantation

Myelinosomes appeared as bleb-like protrusions on myelin sheaths following microelectrode implantation (Figure 3A.). They have been previously shown to exist in neurodegenerative disease and injury models [35, 67, 73]. Growing evidences suggest that the formation of myelinosomes could be caused by either out-folding of focal myelin proteins [73, 74] or axonal blebs underneath the sheath [67, 75, 76]. Qualitatively, there was high level of myelinosomes near the brain-

electrode interface 1h following implantation. These myelinosome structures are hard to study in traditional immunohistochemical staining since they shrink and disappear in post-mortem tissue [35]. These myelinosomes were also observed in Layer I of the contralateral tissue, albeit at substantially lower levels, and most likely due to craniotomy-related injury. Therefore, to examine the effect of chronic implantation injury on myelinosome formation in Layer I over time, contralateral myelinosome density was used as a control to normalize craniotomy injury.

Acutely, there were high densities of myelinosomes near the implanted probe, but this greatly decreased over time and remained low for the duration of the 28-day study (Figure 3B). This density was significantly elevated 0-50 μm from the probe in the first 3 hr post-implantation (*$p<0.0001$)*. By 12 hrs, normalized myelinosome density propagated steadily up to 100 μm away and maintained significantly high levels 0 – 100 μm until 72 hr. Myelinosome density then dropped to control levels by d7 and it remained steady until d28 post-implantation, where the control group of craniotomy window in contralateral hemisphere represented myelinosome density within the most distant bin 225 – 250 μm from the probe surface (Figure 3C; two-way ANOVA with Dunnett's post hoc, $p < 0.01$). Distinct temporal patterns of normalized myelinosome density showed that the peak of myelinosome density within 50 μm at 1hr and 9hr post-insertion exceeded densities at 72 hr. This contrasts with normalized myelinosome density between 50 – 100 μm away from the probe, which gradually increased over time until 72 hr post insertion (Fig. 3D). To characterize the overall spatiotemporal pattern of normalized myelinosome distribution, linear regression was applied to reveal a general trend of myelinosome formation with distance from the probe surface at each time point (Fig. 3E). Regression coefficients, slopes, and y-intercepts were represented as spatial gradient and proximal density, respectively, and plotted as a time series. There was significant, biphasic difference in normalized myelinosome distribution from 1hr to 28 days post-insertion. Two significant transitions in spatial gradient and proximal density occurred at 12hr and 72hr post-insertion. This indicates that there were high levels of myelinosomes near the implant during the initial 12hr following insertion, and then it reduced to moderate levels, but spread further away from the probe between 12hr to 72hr. Lastly, myelinosomes decreased over 3-14 days post insertion.

When tracking individual myelinosomes over time, we observed that the diameter was dynamically changing (Fig 4A). Myelinosomes first appeared as small, highly fluorescent bleb-like structures on myelin processes near the surface of the microelectrode. The diameter of myelinosomes steadily increased from 3h to 12h following implantation injury. Eventually, myelinosomes began to shrink and flatten, which coincided with a decrease in length of the associated myelin sheath, implying that myelinosome formation can precede degeneration of adjacent myelin processes following microelectrode implantation. To investigate changes in myelinosome diameter over both acute and chronic timescales, normalized myelinosome diameter within 100 μm from the implant were quantified over time. A significant peak in myelinosome diameter within 25 μm from the implant occurred at 3 hr post-insertion, followed by a delayed decrease at 24 h post-insertion (Figure 4B; two-way ANOVA with Bonferroni-corrected t tests, $p < 0.05$). Additionally, there was no significant difference in regression slope coefficients of normalized myelinosome diameter across time, which remained consistent around contralateral levels (Fig. 4C).

While myelinosomes eventually disappeared, it is interesting to note the relationship between myelinosome disappearance and myelin degeneration (Fig. 4A, 4D). Qualitative images show that the loss of individual myelinosomes led to local degeneration of associated myelin sheaths, observed as a decreased in length of the myelin segment. However, some myelinosomes disappeared without myelin sheath degeneration, suggesting that early myelin injury from myelinosomes can be repaired under the right conditions. Examining the probability of demyelination in respond to individual myelinosome loss showed that the attached myelin processes were prone to degenerate ($69.05 \pm 11.13\%$), which was significantly higher than surviving myelin sheaths ($30.95 \pm 11.13\%$, paired t-test, $p < 0.01$). Together, these results suggest that myelinosomes are early indicators of myelin injury in response to microelectrode implantation and tend to induce demyelination within the surrounding cortical tissue.

3.3 Progressive demyelination at the electrode-tissue interface over time

Myelin processes provide electrical modulation on signal transmission and metabolic support through direct contacts with neuronal compartments. Evidence has shown that induced systemic demyelination can result in deficits in neuronal firing properties, synaptic oscillations, and laminar communication, which are recorded by microelectrodes [47], emphasizing the necessity to understand how implantation injury affects surrounding myelination. Previous, studies using postmortem immunohistochemistry demonstrated that demyelination occurs at the microelectrode interface [77, 78]. However, immunohistochemical staining provides a snapshot only at one time point and prevents the ability to track dynamic changes in the tissue over time [79]. Here, we used two-photon microscopy to track the time course of demyelination and myelin distribution as a measurement of total myelin length normalized against the contralateral hemisphere (Fig. 5A).

The heatmap of normalized myelin density near the probe over 28 days demonstrated that demyelination progressed mainly within 100 μm from the chronic implant (Fig. 5B). Temporal patterns in normalized myelin density over chronic periods further confirmed significant reductions in normalized myelin density within 25 μm bins from 72h to day 28 post-insertion (Fig. 5C; two-way ANOVA with Dunnett's post hoc with 1h normalized myelin density as control group, $p < 0.05$). Spatial patterns in normalized myelin density within the first 100 μm showed significant differences between each 25 μm bin, indicating demyelination propagates starting at the interface but progressed to distal cortical tissue (Fig. 5D; plotted as mean with 95% confidence intervals; likelihood ratio test for group-wise comparisons).

Similarly, general spatiotemporal patterns in normalized myelin density was quantified using the coefficients of linear regression on distance, spatial gradient (slope) and proximal density (Y-intercept) over time. The time course of these coefficients revealed the remarkable transition in myelin distribution from contralateral levels. These results suggest that myelin density distributed evenly during the first 48 h post-insertion but led to proximal loss at chronic day 28. (Fig. 5E). Significant changes in spatial gradient and proximal myelin density accelerated at 72 hr and potentiated 14 days post-insertion (one-way ANOVA with Tukey post hoc, $p < 0.05$). To investigate temporal correlations between myelinosome density and demyelination during implantation, the time course of percent change in myelinosome and myelin density between two consecutive time points was plotted over time (Fig. 5F; one-way ANOVA with Turkey post hoc, $p < 0.05$). Myelinosomes rapidly increased and then decreased, which coincided with significant demyelination, implying there is a temporal order between myelinosome transients and myelin loss.

Next, to determine the severity of early morphological myelin injury following implantation, the number of myelinosomes on each associated myelin sheath was quantified as an index of myelinosome/myelin ratio. Generally, the distribution pattern of the myelinosome/myelin ratio is similar to myelinosomes, with a high ratio near the electrode-tissue interface during acute implantation while low during chronic implantation (Fig. 6A). Spatial patterns of normalized myelinosome/myelin ratios demonstrated significantly high levels within 50 μm from the implant at day 1 and then increased in distance up to 100 μm until day 5 post-insertion (Fig. 6B; two-way ANOVA with Dunnett's post hoc; control group: 225-250 μm bin). Interestingly, there was a significant increase in normalized myelinosome/myelin ratio at 0-50 μm compared to 225-250 μm bins at day 10, suggesting that early myelin injury is a precursory event to demyelination that occurs by day 10. Low levels of myelinosomes in Fig. 3 and progressive loss of myelin density at day 14 in Fig. 5 may further suggest that the relatively large number of myelinosomes at day 10 is a critical time point of early myelin injury. The temporal patterns of normalized myelinosome/myelin ratios demonstrated a decrease in ratio over time (Fig. 6C; two-way ANOVA with Dunnett's test, control group: d28). The ratio of spatial gradient and proximal density as linear regression slope and Y-intercept, respectively, showed that a significant transition in spatial distribution occurred between day 7 and 14 post-insertion (Fig. 6D; one-way ANOVA with Turkey post hoc). In general, myelinosome formation is an indicator of early myelin injury prior demyelination, which primarily increases at 72h post-insertion and progresses with time near the electrode-tissue interface.

3.4 Oligodendrocyte soma dynamics near the implant during chronic implantation

Oligodendrocyte somas appeared deformed in cortical tissue next to implanted microelectrodes (Fig. 7A). Disappearance of fluorescent-labeled oligodendrocyte soma between time points was an indication of oligodendrocyte soma degeneration following implantation. However, oligodendrocyte precursor cells (OPCs) exist as a reservoir for oligodendrocytes after demyelination injury. While OPCs do not express the *Cnp* promoter and are not fluorescently labeled, differentiation from OPCs into mature oligodendrocytes can be identified as an increase in fluorescence intensity over time. Therefore, oligodendrogenesis at the tissue-electrode interface could be identified using vascular landmarks and other pre-existing oligodendrocytes (Fig. 7B). These observations indicate that the oligodendrocyte population responds dynamically through degeneration and regeneration around the implanted probe. To examine how implantation injury perturbs the balance of oligodendrocyte turnover, dynamic oligodendrocyte populations were divided into degenerated or newly differentiated subgroups binned according to distance away from the probe. Statistically significant differences between degenerated and newly differentiated oligodendrocytes indicated a high loss of oligodendrocyte soma and inhibition of regeneration within 50 μm from the implant (Fig. 7C; unpaired multiple t test, $p < 0.0005$). A significant drop in the rate of change in overall oligodendrocyte density per day suggested that 72h post-insertion is a temporal landmark for oligodendrocyte loss in response to implantation injury (Fig. 7D; one-way ANOVA with Bonferroni corrected t-test comparisons, $p < 0.0001$). The cumulative percentage of changes in oligodendrocyte density relative to 1h post-insertion also confirmed this significant increase in oligodendrocyte degeneration at 72h (Fig. 7E, one-way ANOVA with Bonferroni corrected t post hoc, $p < 0.05$). While degeneration in oligodendrocytes primarily occurred within 72h, there was an increasing trend in oligodendrogenesis during chronic time periods. In order to identify if damage induced by

microelectrode implantation is initiated along myelin processes or oligodendrocyte somas, temporal patterns were quantified as the rate of change between consecutive time points (Fig. 7F). Interestingly, the results showed a convergence of demyelination and oligodendrocyte loss at 72h post-insertion, implying simultaneous degeneration of oligodendrocyte structures, both soma and myelin processes, during the acute inflammatory phase following microelectrode implantation.

Interestingly, we observed a morphologically distinct subtype of oligodendrocytes, referred to here as perivascular oligodendrocytes, located distinctly around blood vessels (Fig. 8A). These perivascular oligodendrocytes have been shown to be essential for maintaining vascular integrity and regulating blood flow in order to support axonal activity [80, 81]. Deficits in perivascular oligodendrocytes result in neuropathology related to blood brain barrier dysfunction and reduction of metabolic rate [80, 81]. We determined that 34.37±12.87% of identified oligodendrocytes in our images were classified as this perivascular subtype with an inter-edge distance (between cell soma and the nearest blood vessel) less than the minimal pixel resolution (0.4 μm/pixel). Moreover, 54.99±8.53% of these perivascular oligodendrocytes were located on capillaries (Fig. 8B-C). Figure 8D is a time-series example of a perivascular oligodendrocyte near the electrode-tissue interface gradually losing fluorescent intensity, implying oligodendrocyte degenerating. Compared to the total oligodendrocyte population within the imaged tissue volume, perivascular oligodendrocytes had an increased susceptibility to degenerate compared to non-perivascular oligodendrocytes near the implant (Fig. 8E). Implantation injury triggered a significant increase in perivascular oligodendrocyte degeneration within 250 μm away from the probe compared to distal control regions (> 250 μm), implying perivascular oligodendrocytes are more vulnerable to implantation-induced damage (Fig. 8F). Additionally, newly differentiated perivascular oligodendrocytes were observed to subsequently myelinate axons, indicating a success in regeneration from OPC to mature myelinating oligodendrocyte at the electrode interface (Fig. 8G). However, we also observed instances of oligodendrogenesis followed by subsequent degeneration without myelin sheath formation (Fig. 8H).

4. Discussion

The current challenge impeding wide clinical application of intracortical microelectrodes is the gradual loss of detectable brain signals over time. Specific depletion of oligodendrocytes and myelin, which modulate signal transmission and facilitate metabolic support, resulted in reduced functional recording performances. Given that the optimal recording radius of each contact site on a microelectrode shank is approximately 50-140 μm from the electrode [82], it is important to characterize the spatial and temporal dynamics of oligodendrocyte and myelin activity within this radius following implantation of a microelectrode array. Two-photon microscopy enables real-time mapping of oligodendrocyte activity proximal to implanted microelectrodes compared to traditional modalities such as immunohistochemical staining and electrophysiology. By using two-photon microscopy within a CNP-EGFP transgenic mouse model, we observed morphological signs of acute injury in myelin, progressive demyelination, oligodendrocyte impairment, as well as potential wound healing and regeneration around the intracortical neural electrode over a chronic 4-week implantation period. Given the significance of myelin within neural circuits [47], a comprehensive spatiotemporal mapping of oligodendrocyte and myelin dynamics can uncover novel insights on the chronic decline of functional electrophysiological performance. Furthermore, this study highlights potentially novel targets for intervention focused on mitigating damage to oligodendrocyte structures in order to improve long-term functional recording.

4.1 Structural dynamics of oligodendrocytes during acute injury (0-12h following insertion)

Traditional linear intracortical microelectrode arrays are made of stiff silicon materials compared to soft brain tissue which results in local mechanical tissue distortion following insertion [68, 83]. Penetration of stiff microelectrodes also rupture the blood brain barrier [83], elicit abnormal patterns of neuronal activity [67], and trigger immediate microglial activation during initial insertion [37]. These biological responses, which occur within 12h after insertion, are characterized as an acute insertion injury that can contribute to neuroinflammation and recording degradation. In this study, we determined that insertion injury also negatively affects oligodendrocyte lineage structures with morphological changes at the tissue-electrode interface over the acute time periods.

Immediately following insertion, myelin and oligodendrocyte somas become strained (Fig 2B, 2D), with the angle of strain oriented along the direction of the probe (Fig 2B, 2E). Myelinosomes, protruding blebs on myelin sheaths, appear immediately near the implanted probe (Fig 3A). Local myelin outfoldings, which result in myelinosome formation, were first observed in animals with experimental autoimmune encephalomyelitis (EAE), a multiple sclerosis model [73]. Blebbing structures were also recently observed in a CNP-EGFP animal in response to brain injury during 1h and 3h following acute implantation [35]. Interestingly, neurite blebs following microelectrode implantation were also reported [67], which possibly contribute to this swollen morphology in ensheathing myelin. However, myelinosomes discussed in

this paper are local bulb-like structures on the surface of myelin sheaths in CNP-EGFP mice, which does not distinguish blebbing from myelin or the underlying neurites.

Myelin orientations suggest that mechanical strain may lead to greater levels of myelinosome formation, indicating that the mechanical force from insertion is associated with the severity of myelin injury. These myelinosomes have been characterized as an early marker of morphological injury in myelin following similar brain injuries [35] and in neurodegenerative disease [73]. The rate of myelinosome formation and size of myelinosomes are indicative of the degree of myelin injury. Figure 3C and 4B suggest that insertion causes considerable myelin injury at the electrode-tissue interface and that myelin injury is more severe with increasing proximity to the implant. However, myelin processes wrap around axons and the GFP+ fluorescence only labels the myelin membrane. Therefore, a limitation of two-photon observation of the CNP-EGFP transgenic model is the inability to distinguish whether the observed protrusion originated either from myelin membrane dilation or underlying axonal blebs. In previous publications, axonal blebs were also observed *in vivo* as a sign of early axonal damage in response to microelectrode implantation injury [67]. Future studies should address this by developing transgenic models that label both myelin sheathes and underlying axons to simultaneously track axonal and myelin blebs in response to chronic implantation injury.

While substantial formation of myelinosomes represented acute structural injury on the surrounding myelin, the shape of oligodendrocyte somas was preserved following initial deformation at the tissue-electrode interface. However, even if oligodendrocyte somas did not change shape, it does not exclude the possibility that their cellular homeostasis may be disrupted. This could be due to metabolic deficiency [84], disruption in ion balance [85], or apoptotic signaling [30] within a toxic neuroinflammatory environment. Taken together, mechanically-strained myelin and oligodendrocytes as well as appearance of myelinosomes are representations of acute tissue injury that may decrease the biocompatibility and recording performance of implanted microelectrodes.

4.2 Myelin and oligodendrocyte damage during acute inflammation (12-72h following insertion)

During the acute inflammation phase within the tissue-electrode interface, activated microglia cover the implant surface [31], reactive astrocytes start to encapsulate via an outer glial layer [30], and vascular damage occurs [30]. While these biological responses persist following the initial implantation, electrophysiology recording metrics, especially single-unit (SU) amplitudes, SU signal-to-noise ratios (SNR), and multi-unit (MU) firing rates are shown to decrease dramatically 3 days post-insertion [16, 47]. While formation of an encapsulation layer by activated microglia and reactive astrocytes could increase the resistance to signal transmission and contribute to impaired signal quality, injury of oligodendrocytes that are responsible for modulating neuronal signal conduction velocities and metabolic support are likely to be associated with declining device performances [47].

The distribution of myelinosomes surrounding the probe demonstrate a distinct spatial pattern during the acute inflammation period relative to the initial insertion injury (Fig. 3E). Although the level of myelinosomes near the probe during acute inflammation is lower relative to the initial 12h injury (Fig 3D), myelinosome formation increases over distances up to the effective recording radius for individual contact sites (50-140 um) (Fig 3C). This level of myelinosome formation is associated with the extent of myelin sheaths experiencing myelinosome injury (Fig 6B). Together, this increased range of myelinosome distribution during acute inflammation implies that inflammatory cascades during implantation injury propagates and expands the area of myelin injury, which is likely due to homeostatic dysfunctions caused by the initial mechanical trauma [86], a high gradient of proinflammatory cytokines and chemokines [39], and elevated phagocytosis by activated glia that have shown to be highly aggregated around the probe by 72h post-insertion [31].

Individual myelinosomes can progress over time and, in turn, lead to myelin loss (Fig 4A). A majority of myelinosomes formed at the tissue-electrode interface inevitably lead to a corresponding loss in myelin (Fig 4E). This implies that myelin suffering greater morphological damage, as indicated by myelinosomes, are more likely to experience sequential demyelination. Activated microglia and macrophage engulfment has been suggested to mediate myelinosome degeneration as their processes are shown to be in close apposition to myelinosomes [73]. Additionally, large amounts of activated immune cells have been shown to aggregate around the implant during acute inflammation [31], which may explain the greater proportion of myelinosome degeneration followed by myelin loss over greater distances from the implanted probe. Rapid increases in myelinosome density precede demyelination and a substantial amount of myelinosomes result in a significant myelin loss at 72h post insertion (Fig 5F). This further supports the idea that myelinosome formation close to the probe may be an early indicator of severe myelin degeneration.

A noticeable loss of myelin within the first 50 μm from the electrode and a decrease in oligodendrocyte soma occurs 3 days post-implantation (Fig. 5C, 5E, 7D). Additionally, the loss of oligodendrocyte soma population is associated with a substantial loss in pre-existing oligodendrocytes as well as minimal oligodendrogenersis from oligodendrocyte progenitor cells (Fig 7E). Overall, implantation of intracortical microelectrodes leads to simultaneous degradation of oligodendrocytes and myelin processes at 3 days post-insertion along with increased microglia coverage, astrocyte reactivity, and elevated vessel leakage, suggesting increased cellular and tissue dysfunction near the implanted microelectrode.

Myelin is essential for the transmission of electrical signals along axons and supporting axonal health. We have previously shown that the conditional depletion of oligodendrocytes and myelin can reduce functional recording capability [47]. In this study, we noticed that the initial demyelination and bulk oligodendrocyte loss that occurs at 3 days post-insertion can be correlated temporally with the pattern of decline in recording signal quality previously observed [16, 47]. This suggests that a loss in oligodendrocyte cells and their structural components within the tissue-electrode interface is associated with the loss of functional recording performance.

4.3 Progressive demyelination during early chronic inflammation (3-14 days)

A progressive decrease in biocompatibility and functional recording performance occurs during this early chronic inflammatory period. A prominent increase in reactive astrocytes encapsulating the probe coincides with significantly decreased survival of nearby neurons [30]. Single unit activity (yield, SNR, amplitude), multi-unit activity (stimuli-evoked MU firing rate), and laminar communication (inter- and intra- layer coherence) are substantially decreased up to 14 days post-insertion [16, 47]. Our results demonstrate that the observed pattern of oligodendrocyte degeneration can complement our current understanding of decreased biocompatibility during this implantation period and suggests a potential association with recording performance failure.

Myelinosome injury becomes steady during the 3-14 day inflammation period. Low myelinosome density (Fig 3C, 3E) at 72 hr matches the time when microglia have substantially covered the implant surface [31]. However, we notice that myelinosome densities proximal to the implant slightly increase (Fig 3C) followed by a second peak prior to demyelination at 7 days (Fig 5F). This is likely an early sign of progressive demyelination within the tissue-electrode interface. The number of myelinosomes within individual myelin further confirms that myelinosome-induced myelin injury evokes a similar pattern of demyelination (Fig 6B).

While myelinosome activity is modestly present early during this chronic inflammation period, prominent demyelination spreads both spatially and later progressively near the probe. Demyelination may lead to deficits in signal conduction and myelin-axon metabolic coupling, which may account for the degradation in recording performances including reduced neuronal firing and laminar connectivity early during this chronic inflammatory period. Additionally, myelin loss is persistent over time near the implant (Fig 5E) and coincides with substantial decline in electrophysiological metrics. Interestingly, cortical tissue closer to the probe experiences faster rates of demyelination (Fig 5D). Remarkably, myelin vulnerability to the neuroinflammatory environment near the implant matches the time course of demyelination and neurological dysfunction at 7 and 14 days following stroke [87], suggesting common temporal patterns of inflammatory cascades contributing to decreased myelin integrity and impaired neural circuit function.

Although oligodendrocyte loss early during the chronic implantation period is not prominent, a prior study reported that a significantly large proportion of oligodendrocytes near the implant suffer from increased apoptosis [30]. This indicates that oligodendrocytes may experience a disruption in homeostatic balance within a neuroinflammatory environment and potentially cannot execute normal cellular functions even though their somas are not degenerated. Taken together, persistent and elevated neuroinflammatory responses around the implant exacerbate damage to myelin and oligodendrocyte integrity during 3 to 14 days post insertion. This likely negatively impacts the stability of axonal signal propagation since myelination prevents rapid decay of action potentials during transmission. Therefore, a loss in electrophysiological signals is probably a consequence of myelin damage, critical for signal stability, and gliosis, critical for signal sensitivity.

4.4 Degeneration and wound healing of oligodendrocyte population during chronic immune response (14-28 days)

After 2 weeks of implantation, the glial scar becomes compact and the intensity of microglia and astrocyte activity decreases [88]. Therefore, biological reactions around the implant gradually switch from insertion-induced inflammation to a chronic immune response that is considered to represent injury stabilization following immune glia activity [88]. However, recent evidence suggests additional contributors are involved during this period, including degeneration of the

neurovascular unit, significant bleeding, and increased neuronal apoptosis [30]. Here, we notice there is persistent myelin loss up to 100 μm away from the probe (Fig 5C). However, previous electrophysiology recordings in mice showed functional recovery at 28 days post-insertion, with an increase in neuronal firing [16, 47]. This paradoxicality can potentially be explained by the removal of myelin debris, which acts as an inhibitor of axonal regeneration, and would be beneficial for functional tissue recovery as previously suggested [89, 90]. We have shown that there is a prominent decrease in functional recording performance at 6 weeks following insertion and demonstrated electrophysiological metrics that are comparable to a myelin-depleted model [47]. In turn, this could explain why, across all neurotechnologies, it is challenging to record single-units from hippocampal CA1 beyond 4-6 weeks after chronic implantation, which requires implantation through the callosum cassette, the white matter tracks that project to CA1 neurons [16, 47, 68, 91-93]. Therefore, preparation of *in vivo* oligodendrocyte and myelin observation for more than 4 weeks may help to determine the ultimate fate of myelination, either degeneration or repair, following brain implantation injury.

Chronic microelectrode implantation results in persistent degeneration of pre-existing oligodendrocyte soma near the implant (Fig 7C, 7E). Remarkably, this region corresponds to the region of tissue that experiences mechanical stress, which implies that mechanically strained oligodendrocyte somas suffer from impaired integrity and, in turn, have a diminished ability to resist inflammatory injury. Specifically, we observe a subtype of oligodendrocytes that are in close juxtaposition to blood vessels (Fig. 8A, 8B). This population of perivascular oligodendrocytes have been suggested to facilitate oligodendrocyte-endothelial interactions that maintain individual cellular functions and promote angiogenesis and oligodendrogenesis through molecular mediators such as brain-derived neurotrophic factor (BDNF), vascular endothelial growth factor (VEGF), and adrenomedullin (AM) [81, 94]. Dysfunction or degeneration of perivascular oligodendrocytes has been associated with cognitive impairment in schizophrenia [80]. Degeneration of perivascular oligodendrocytes were observed alongside loss of vasculature close to the implant, which suggests that damage to perivascular oligodendrocytes at the tissue-electrode interface is associated with a loss of capillary perfusion. Implantation leads to significant damage within perivascular soma (Fig 8E, 8F), which in turn may impair capillary integrity. Previous evidence supports this hypothesis by demonstrating substantial IgG leakage and diminished vascular structures near the implant at 28 days post-insertion [30].

Formation of oligodendrogenesis with extending myelin processes suggests a successful differentiation of precursor cells into mature myelinating oligodendrocyte at the tissue-electrode interface (Fig 7B). Previous studies have shown that oligodendrocyte precursor cells (OPCs) can receive neuronal signaling through glutaminergic and GABAergic pathways and as a result, differentiate into myelinating oligodendrocytes to support neuronal survival [41]. Enhanced OPC proliferation and differentiation have been demonstrated to promote functional recovery following brain injury [95]. Therefore, wound healing processes related to myelination and oligodendrogenesis around the microelectrode implant are likely to contribute to improvements in functional recording performances. Interestingly, new myelinating oligodendrocytes appear proximal to blood vessels at the tissue electrode interface (Fig 8G), which matches previous evidence demonstrating close proximity of OPCs with vasculature near the implant [31] and suggests a potential for differentiation of OPCs into mature myelinating oligodendrocytes in apposition to blood vessels. Both OPCs and oligodendrocytes have been shown to regulate blood brain barrier permeability and direct angiogenesis [41, 80, 81], which can influence the chronic stability and reliability of functional devices [68]. However, without further studies the behavior and function of perivascular oligodendrocytes near implanted microelectrodes remains unclear.

Regeneration of oligodendrocytes mainly occurs during chronic time periods (Fig 7E). This is consistent with the time course of late OPC differentiation into oligodendrocytes following brain injury [30, 96-99]. However, it is indicated that oligodendrogenesis close to the implant via OPC differentiation is suppressed (Fig 7C), which is likely due to the encapsulating gliosis and neuroinflammatory signaling cascades that drive OPCs to differentiate into reactive astrocytes at the tissue-electrode interface. While abundant OPCs have been shown to become activated and migrate toward the implant within 72h following insertion [31], the time course of OPC differentiation into reactive astrocytes has been implicated to occur prominently during the early inflammation period [30] while OPCs may differentiate into new oligodendrocytes during the chronic immune response period. Targeting OPCs for preferential differentiation into myelinating oligodendrocytes has been shown as an effective intervention to improve functional behavior during neurological disorders [100]. Appropriate external stimuli such as pharmaceutical and/or mechanical cues on OPCs may increase differentiation of the myelinating oligodendrocyte population near the implant, preserving functional neural circuits at the electrode-tissue interface. Promising intervention candidates such as Fingolimod, an FDA approved drug to treat multiple sclerosis, could improve the limited regenerative capacity of oligodendrocytes proximal to the implant. Therefore, enhancement of OPC differentiation into mature myelinating oligodendrocytes may promote wound healing in response to implantation injury and ultimately improve device biocompatibility and chronic signal fidelity.

While brain tissue has some limited capacity to regenerate after injury, wound healing attempts around the probe are not always successful. Failure for oligodendrocytes to regenerate following microelectrode injury (Fig 8H) suggests that the neuroinflammatory environment caused by implantation results in inefficient differentiation of OPCs or viability of newly differentiated oligodendrocytes, which may compromise the ability maintain normal functions of nearby neurons. However, mechanisms underlying the degeneration of newly differentiated oligodendrocyte around the implant injury remain unknown. Future studies should focus on improving effective oligodendrocyte soma regeneration to improve tissue healing following implantation injury.

4.5 Innate wound healing of myelinating structure as targets for biomaterial design

Innate wound healing after insertion is apparent as a small proportion of myelin can recover from early morphological injury (Fig. 4E). The acute transient myelinosome density observed within 12h before demyelination (Fig 3C, 5E, 6B) suggests that myelin is likely to be resistant to inflammatory injury and can restore cellular homeostasis back to a physiological level [101]. Myelinosomes are the morphological representation of early myelin injury, but oligodendrocyte lineage structures are suggested to have the innate ability to self-repair in a calcium-dependent manner [101, 102]. Our results show that the consequence of myelinosome development is primarily the degeneration of the associated myelin sheath, which is hypothesized to contribute to the degradation of functional recording capability. Therefore, enhanced repair of myelinosomes during the acute injury may mitigate progressive myelin degeneration and translate into increased tissue health and recording performance.

Oligodendrocytes, myelin, and OPCs have the potential to act as promising novel targets to promote integration of brain tissue with microelectrode devices and enhance long-term device performances. Previous studies have shown that oligodendrocyte activity can be manipulated by external stimuli such as pharmaceutical cues and mechanical strain [103, 104]. Biomaterial strategies focused on these aspects are hypothesized to improve the integrity of local oligodendrocyte soma and myelin, and thereby functional device capabilities. One potential strategy to preserve myelin structure could be application of a biomaterial coating encapsulating a drug specific for myelin repair. Drug-eluting polymer coatings are hypothesized to modulate oligodendrocyte behavior by passive diffusion or controlled release into the surrounding tissue [105]. Myelin integrity may be preserved by loading drugs or modifying surface chemistries that aim to inhibit NMDA receptors and reduce calcium influx [106], reduce protease calpain activation to decrease cytoskeleton disorganization [107-109], or mitigate oxidative stress to protect mitochondria activity [110]. These myelin-repairing drugs can be delivered via direct functionalization onto the surface of the device or tethered with a polymer coating [23]. While drug molecules directly attached to the probe merely interact with surface-adherent cells, drug-loading polymer coatings can have release effects over a greater spatial range away from the probe surface. Myelin-repair drugs can also be administered to the electrode-tissue interface through uncharged passive substrates such as polyester poly(d,l-lactide-co-glycolide) (PLGA) [111]. PLGA is a common biodegradable material that can continuously release loaded molecules without any induction of inflammatory responses [112]. Alternatively, conductive polymer coatings can be used to achieve controlled release of loaded myelin-repair drugs via electrical stimulation. The conductive substrates, such as poly(ethylene dioxythiophene) (PEDOT), have been shown to be electrochemically stable over the device surface and biocompatible during chronic stimulation [27]. The efficacy and stability of conductive polymer coatings with anti-inflammatory drugs could enable this technology to become a potential modification to improve tissue responses while still preserving the device's electrical properties.

An alternative strategy to reduce myelin injury may be to minimize mechanical strain induced by insertion, which can be resolved by changing stiffness, geometry, or the size of the implant [23]. Our results demonstrate that mechanical strain on oligodendrocyte lineage structures is correlated to substantial myelin loss and soma degeneration. Flexible devices which mimic the elastic modulus property of native brain tissue is thus hypothesized to reduce morphological distortion and severe degradation of oligodendrocytes. For example, hydrogel coatings absorb water and provide stiff devices with similar mechanical properties relative to native brain tissue [113, 114]. Since the brain is constantly floating due to bodily motions and breathing [115], hydrogel coatings could make anchored devices more flexible in order to minimize re-injury during minor displacements of the brain. However, flexible hydrogels increase tissue drag during insertion and can reduce the functional signal quality due to increased distance to the nearest neurons [23]. An alternative strategy to flexibility is reducing material dimensions such as with carbon fiber microelectrodes. Advanced carbon fiber microelectrodes have subcellular cross-sectional areas with sufficient electrical properties packaged in a much smaller device volume compared to traditional silicon microelectrodes, which can result in decreased tissue displacement and mechanical strain to surrounding brain tissue [21, 23]. These ultrasmall microelectrodes result in decreased gliosis and improved neuronal health and device recording performances [21]. Therefore, the implantation of microelectrodes with reduced dimensions is

implied to enhance the integration of functional devices with oligodendrocyte lineage structures essential for signal transmission and neuronal survival within the brain. Furthermore, geometric modifications such as etching the device surface may also be a means to minimize device dimension and cross-sectional area [116]. Etching parallel grooves at the nanoscale can reduce device diameters and mimic dimensions of extracellular environments, which significantly reduces glial encapsulation and improve neuronal survival and functionality over chronic time periods [116]. Furthermore, open- or lattice- structure designs reduces the device volume as well as creates diffusion gaps between tissue and device surface to increase biocompatibility and mitigate device-induced inflammatory injury, and may improve oligodendrocyte health [117].

Conclusion

This study investigates real-time spatiotemporal dynamics of oligodendrocytes and myelin in response to intracortical microelectrode implantation. The formation of myelinosomes, an early morphological indicator of myelin injury, is observed within 72h after insertion. Degeneration of surrounding myelin processes starts at 72h and substantially progresses both spatially and temporally. Loss of oligodendrocyte soma is prominent near the implant acutely but is compensated by limited regeneration of new soma during chronic implantation periods. This study focuses on an oligodendroglial population that has yet to be fully understood within neuroinflammatory cascades and functional outcomes, which provide a more comprehensive understanding of dynamic cellular responses to implant injury. These detailed characterizations of biological activity can guide future interventions to mitigate oligodendrocyte injury and target oligodendrogenesis near the implant. Given the essential impact of oligodendrocytes on supporting neural signals, oligodendrocytes have the potential to be a target for novel intervention strategies aimed at enhancing the stability and reliability of chronically implanted intracortical microelectrodes. Engineering more stable long-term recording capabilities, especially from CA1, will enable neuroscientists to explore new scientific questions, particularly regarding memory and plasticity.

Acknowledgement

The authors would like to thank Franca Cambi for expert consultation, Dr. Tim Harris for valuable discussions, and Kevin C. Stieger for critical review of the manuscript. This work was supported by NIH NINDS R01NS094396 and a diversity supplement to this parent grant as well as NIH R01NS105691, R01NS115707, and R21NS108098, and NSF CAREER 1943906.

Figures

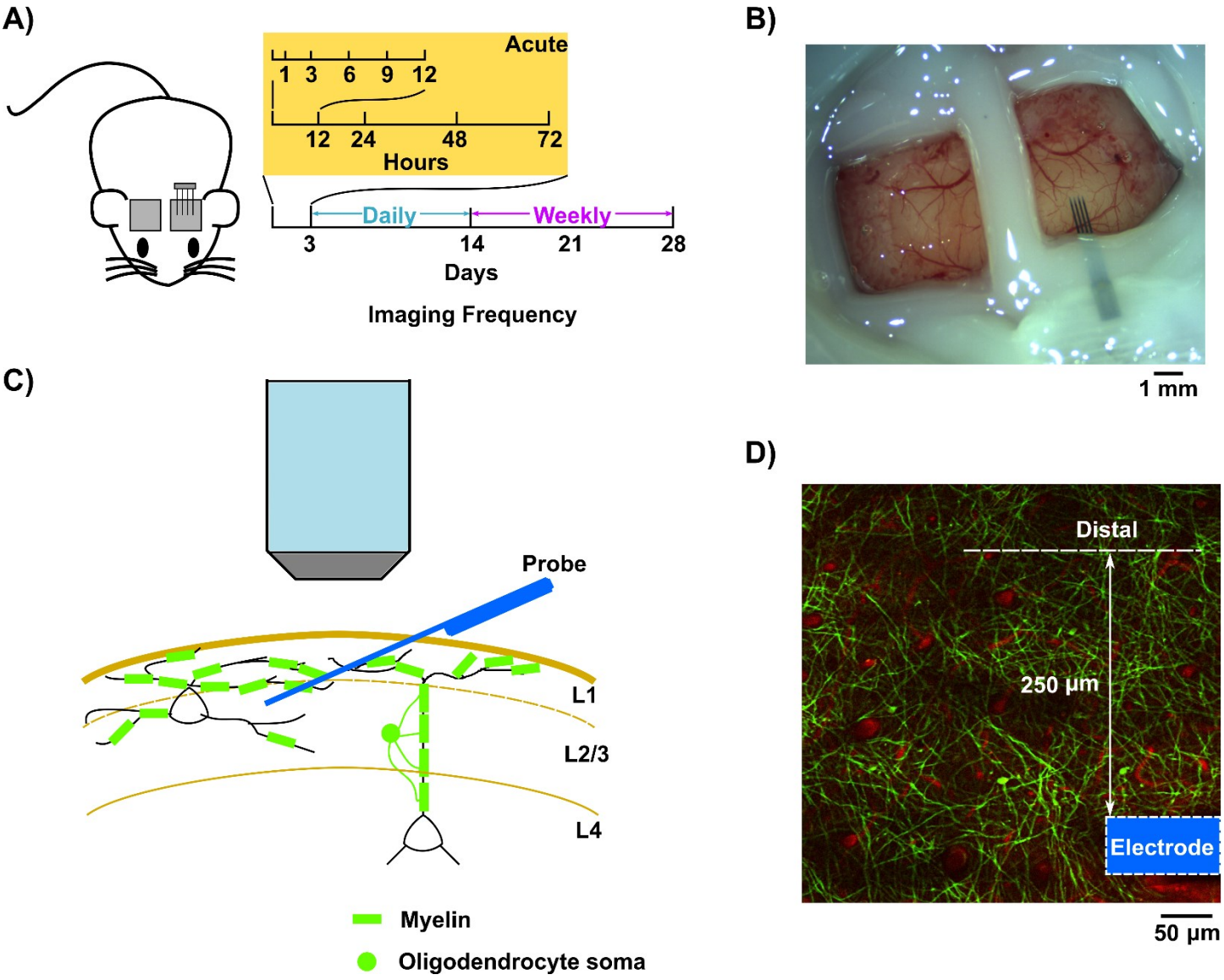

Figure 1: Chronic experimental setup to investigate real-time oligodendrocyte activity within the tissue-electrode interface. A) Schematic for two-photon imaging. After microelectrodes are implanted at 30° angle over visual cortex, CNP-EGFP mice were imaged at 1, 3, 6, 9, 12, 24, 48, 72h following insertion acutely, daily up to 14 days, then weekly until end point at 28 days post-insertion. B) Chronic ipsilateral and contralateral imaging window preparation. C) Microelectrodes penetrated cortical layers with resting depth within Layer II/III, while myelin distribution in the transverse plane is mainly in Layer I. Therefore, the imaging plane to track oligodendrocyte activity is in Layer I. D) Oligodendrocyte dynamics quantified within 250 µm adjacent to the outmost microelectrode shank is considered as the interface response to the implantation (arrow), while the activity beyond 250 µm are quantified as distal activity. The outmost electrode shank is outlined (blue).

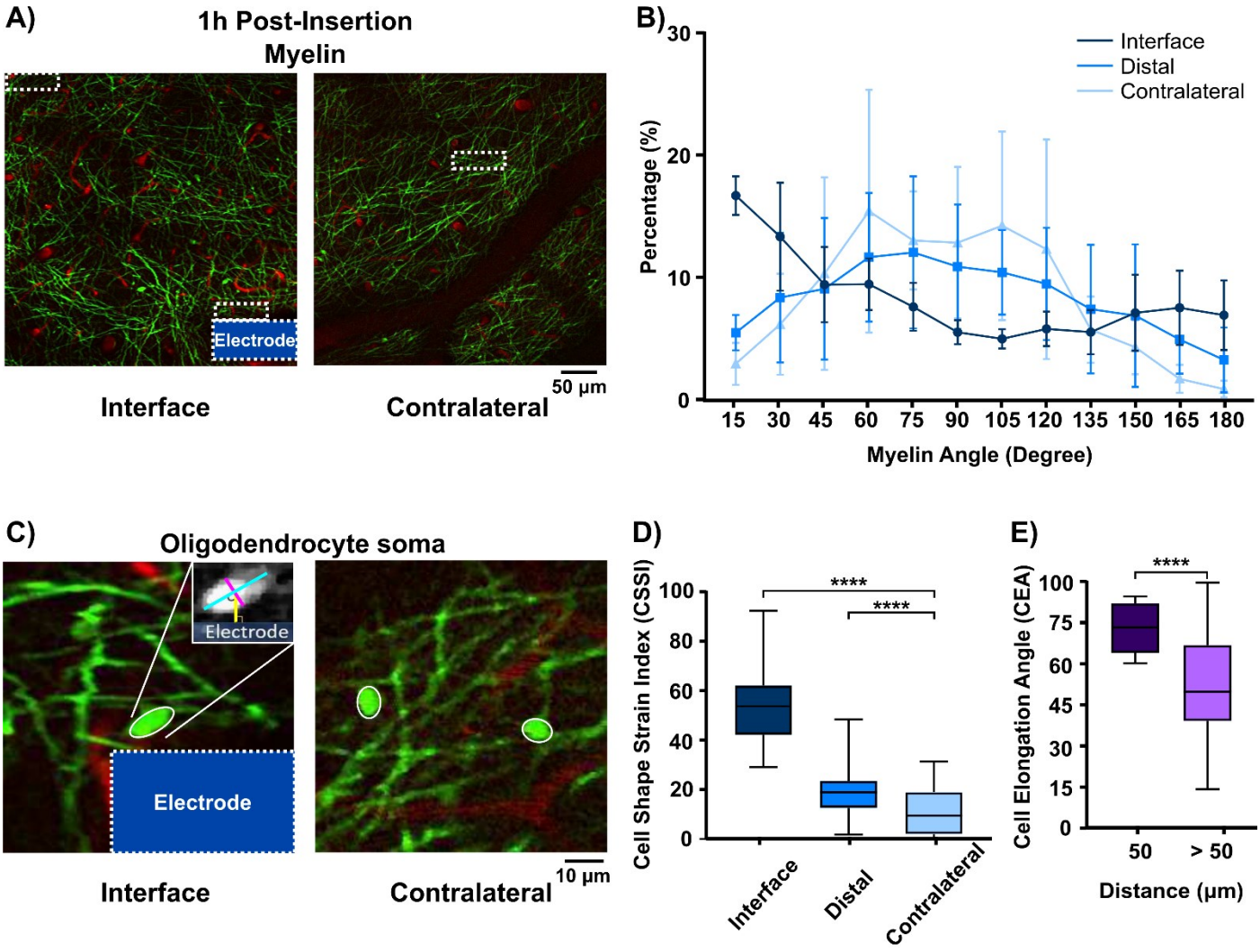

Figure 2. Myelin and oligodendrocytes experience morphological distortion *in vivo* due to microelectrode implantation into the cortex. (**A**) Representative images of EGFP-labeled oligodendrocyte structure and red fluorescently labeled vasculature on the implant and contralateral area 1h following insertion. White dashed rectangles indicate ROIs at the interface, distal regions (> 250 µm away from the implant), and contralateral side. (**B**) Angle distribution of myelin pixels, which indicates the orientation preferences of myelin processes within the ROI. Group-wise significant differences ($p < 0.05$) showed that myelin tended to align parallel to the implant direction (U shaped curve) compared to normally-orientated myelin sheaths at distal and contralateral regions (∩ shaped curve). (**C**) Oligodendrocyte somas adjacent to the implanted probe have a more elliptical shape compared to circular OLs on the contralateral side. Morphology of oligodendrocyte somas is measured by manual elliptic fitting with the major axes (long blue line) and the minor axes (short red line), and are used for calculation of Cell Shape Strain Index (CSSI) and CEA. (**D**) Distribution of OL soma CSSI at electrode-tissue interfaces (≤ 50 µm), distal tissue > 250 µm, and contralateral regions ($p < 0.0001$). (**E**) The direction of elliptic OL soma is measured by the angle between the major axes and a line perpendicular to the implant (yellow line in Figure 2c) and plotted in a box plot for OLs within 50 µm radius from the implant and > 50 µm from the interface ($p < 0.0001$). **** indicates significance at p value small than 0.0001. All data presented as mean ± standard deviation.

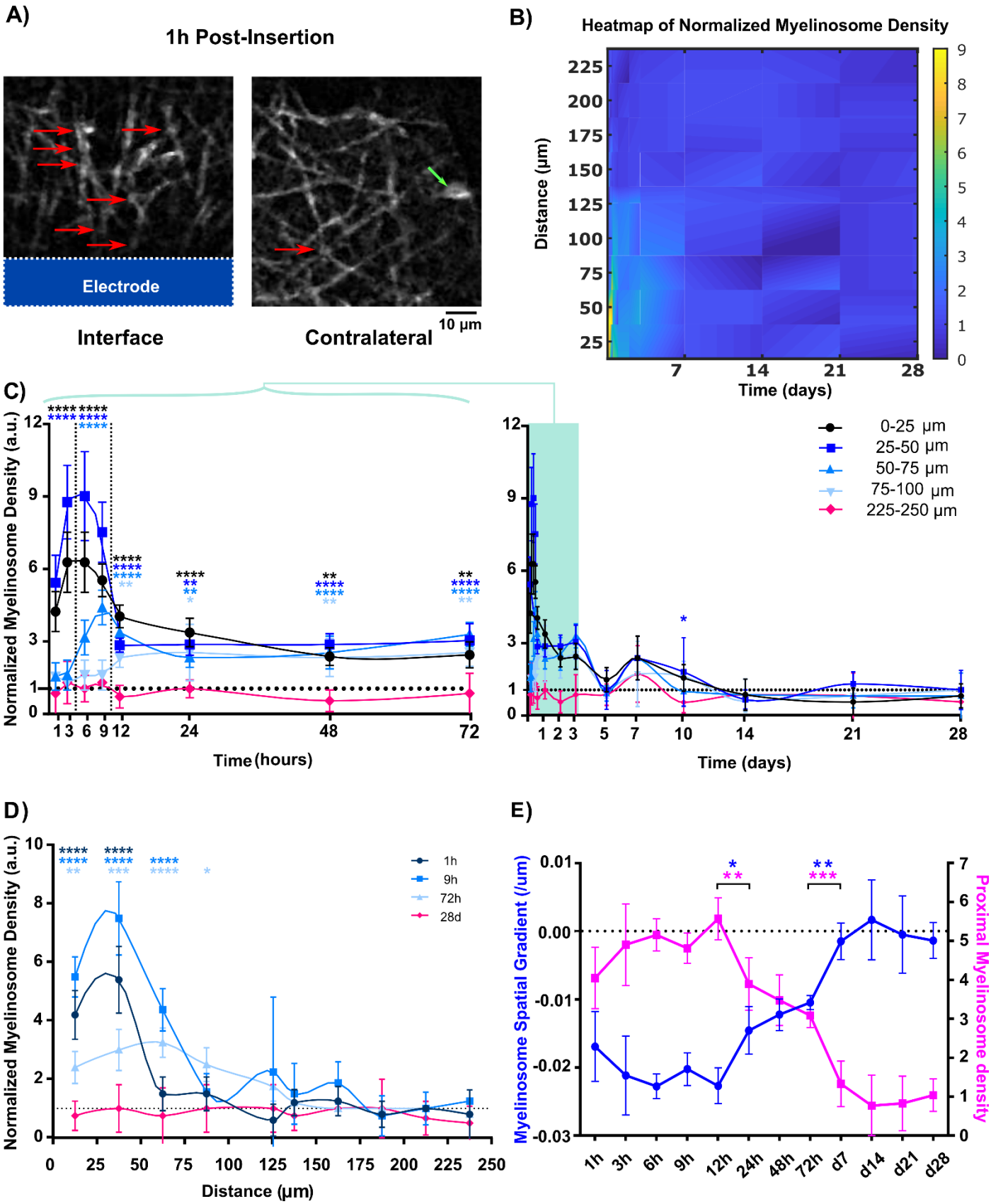

Figure 3. Myelinosomes appeared on myelin processes at the microelectrode interface acutely following implantation. (**A**) Representative images show large numbers of bleb-like protrusions (red arrow) near the implant. In contrast, low amounts of myelinosomes protrusions are observed in the no-implant contralateral regions (green arrow indicates OL soma). (**B**) Heatmap shows the normalized myelinosome distribution from the implant surface over the 4-week implantation period. High levels of normalized myelinosome densities are observed acutely after microelectrode implantation. (**C**) Normalized myelinosome density within 100 µm from the probe at each time point until chronic week 4 post implantation compared to control (225-250 µm bin). Normalized

myelinosome density is high within 50 μm from the probe immediately following insertion, and then gradually expands spatially up to 100 μm from the surface of the implant until 72h post insertion. This activity eventually reduced to contralateral levels following chronic implantation. (**D**) Distinct temporal patterns of normalized myelin density binned 25 μm up to 250 μm away from the surface. Normalized myelinosome density primarily within 100 μm is distinguished from normalized contralateral levels. (**E**) Changes in patterns of linear modeling of normalized myelinosome density with respect to distance over time shows sharp transition in spatial distribution of myelinosomes at the interface at 12-24h and 72h to 5 days post-implantation. In the linear regression model, the regression slope is represented as myelinosome spatial gradient and regression Y-intercept is reported as proximal myelinosome density, showing a sharp transition from skewed spatial distribution acutely to evenly low distributions chronically. (*: $p < 0.05$; **: $p < 0.01$; ***: $p < 0.0005$; ****: $p < 0.0001$) All data presented as mean ± standard deviation.

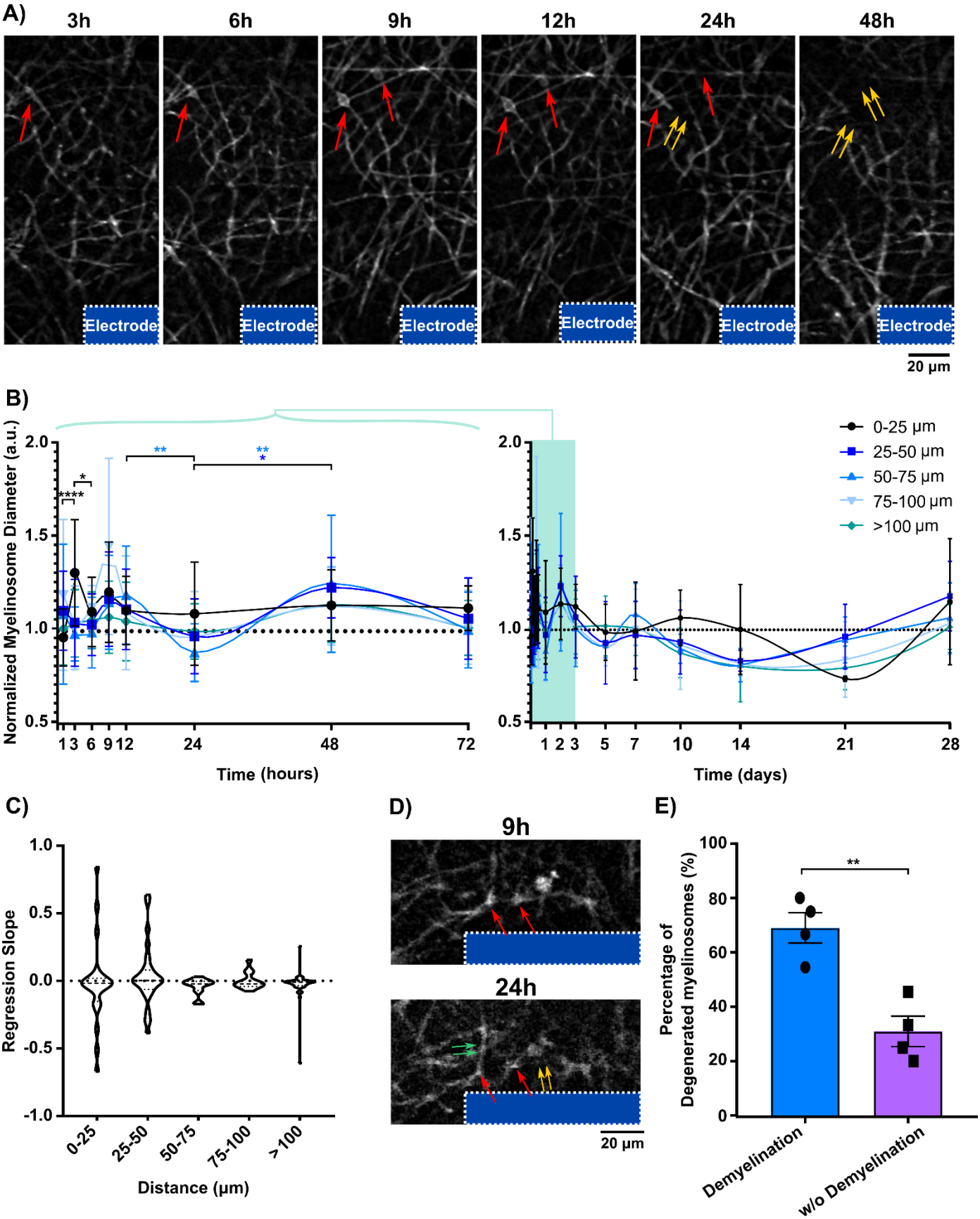
A)
3h
6h
9h
12h
24h
48h
Electrode
20 µm
B)
Normalized Myelinosome Diameter (a.u.)
Time (hours)
Time (days)
0-25 µm
25-50 µm
50-75 µm
75-100 µm
>100 µm
C)
Regression Slope
Distance (µm)
0-25
25-50
50-75
75-100
>100
D)
9h
24h
20 µm
E)
Percentage of Degenerated myelinosomes (%)
Demyelination
w/o Demyelination

Figure 4. Dynamic changes to myelinosome diameter and demyelination at the tissue-electrode interface over time. (**A**) Representative image sequences show individual myelinosomes near the implant (red arrows) dynamically change diameter over time. Disappearance of myelinosomes coincides with the degeneration of adjacent myelin (double yellow arrows). (**B**) Myelinosome diameter normalized to contralateral regions over 250 μm away from the probe, divided into myelinosome active areas in bins of 25 μm up to 100 μm away from the probe surface and resting interfacing region (100-250 μm), reveals a significant peak in diameter at 0-25 μm from the probe surface 3 h post implantation. (**C**) Temporal patterns of normalized myelinosome diameter evaluated by linear regression demonstrate comparable trends of normalized myelinosome diameters within distinct regions over time. (**D**) Degradation of some myelinosomes (red arrow) can lead to subsequent demyelination (double yellow arrows). In contrast, some myelin (double green arrows) segments survive when the adjacent myelinosomes disappear (suggesting potential repair). (**E**) Percentage of myelinosomes associated demyelination and surviving myelin length over the total myelinosomes labeled segments near tissue-electrode interface (≤ 100 μm) demonstrates that the fading of myelinsome tends to be followed by myelin degeneration near the implanted probe. (*: $p < 0.05$; **: $p < 0.01$) All data presented as mean ± standard deviation.

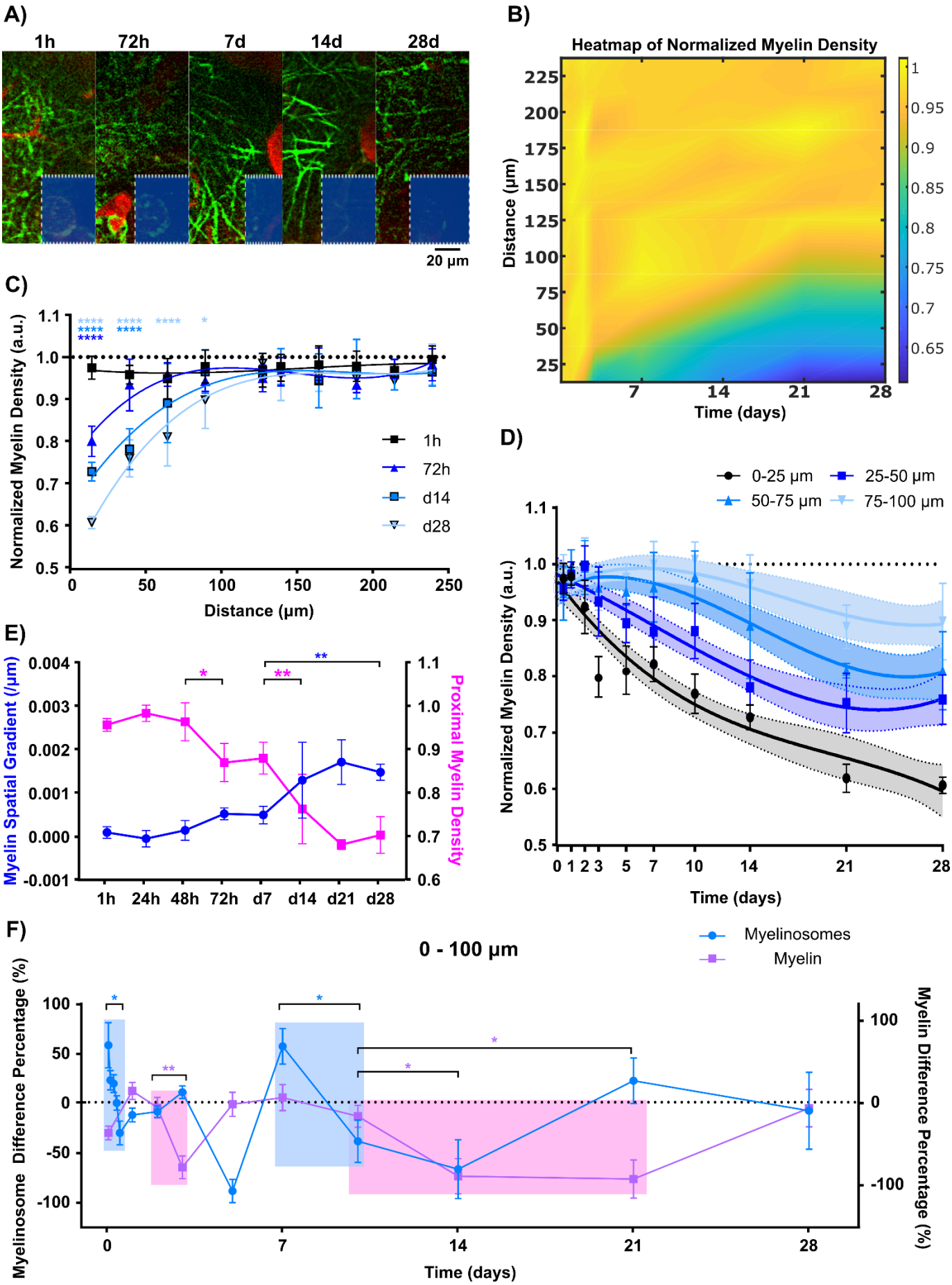

Figure 5. Severe demyelination occurs proximal to the implant over the chronic 4-week implantation. (**A**) Representative time-series (1 hr to 28 days) images show a decrease in myelin distribution (green) near the implant. Red denotes SR101-labeled blood vessels. (**B**)

Spatiotemporal heatmap of normalized myelin density over time. Visible decrease in myelin density is observed near the implant. (**C**) Normalized myelin density per length measurement shows significant myelin reduction occurs close to the electrode-tissue interface initially, but expands over time up to 100 μm away from the implant surface. (**D**) Characterization of myelin density modeled with non-linear third order polynomial (cubic) fitting (95% confidence intervals as shadowed regions). The likelihood ratio test for group-wise significance exhibits distinct spatial profiles of normalized myelin density. (**E**) Linear regression model of normalized myelin density over distance (spatial gradient represents regression slope and proximal density indicates regression intercept) indicates spatial patterns of normalized myelin density at the tissue-electrode interface significantly changes at 72 hr and 14 d following electrode insertion. (**F**) Temporal relationship of normalized myelinosome density and normalized myelin density within 100 μm of the probe demonstrates large decreases in normalized myelinosome density (light blue shadow; significant shift from positive to negative value) is followed by a delayed reduction in normalized myelin density (light pink shadow; significant negative value). Difference in percentage is determined as the difference between two time points over the average value of two time points. Positive difference percentage indicates increase compared to the previous time point, while negative difference percentage shows decline from the previous time point. (*: $p < 0.05$; **: $p < 0.01$; ***: $p < 0.0005$; ****: $p < 0.0001$) All data except (**E**) are presented as mean ± standard deviation. Difference percentage is reported as mean ± standard error for clear visualization.

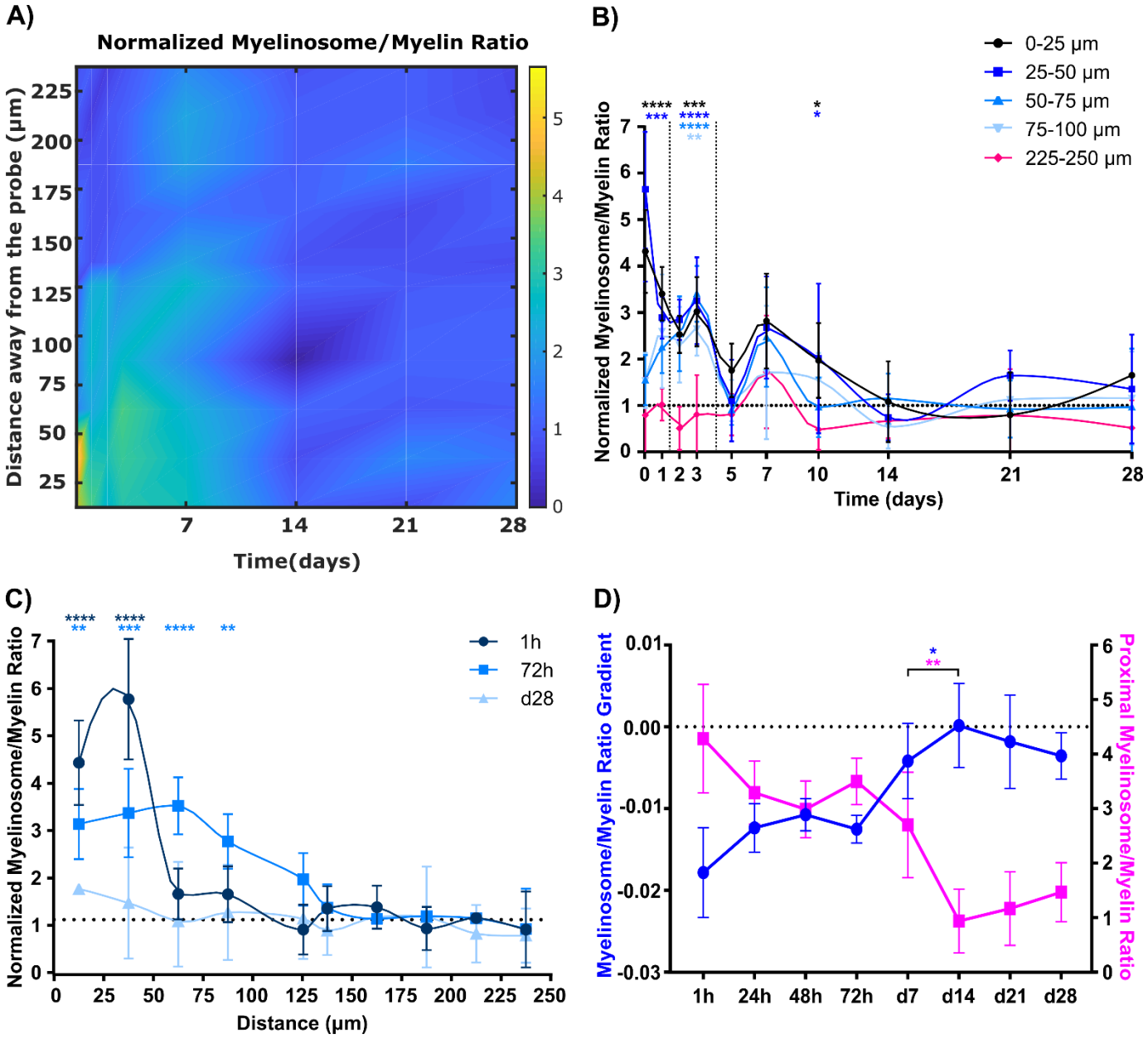

Figure 6: The number of myelinosomes on each myelin segment is high during the acute inflammation period but relatively low over chronic time points. (**A**) Heatmap characterization of normalized myelinosome/myelin ratio shows most myelin segments have multiple myelinosomes acutely near the tissue-electrode interface. (**B**) Spatial representation of normalized myelinosome/myelin ratio per day within 100 μm tissue-electrode interfacing regions. High levels of normalized myelinosome/myelin ratio occur from 50 μm to 100 μm away from the implant during acute phase (<72h post insertion) ($p < 0.01$). (**C**) Temporal variation in normalized myelinosome/myelin ratio from implant surface up to 250 μm away at representation 1h, 72h, and d28 following implantation. Acute

implantation results in significantly high normalized myelinosome/myelin ratio proximal to the implant ($p < 0.01$), while chronic implantation has normalized ratios similar to the contralateral hemisphere. (**D**) Linear regression modeling quantifies changes in spatiotemporal distribution of normalized myelinosome/myelin ratio significantly occurs at d7 post insertion, shows that abrupt change in myelinosome/myelin ratio spatial distribution to low, evenly distribution (*: $p < 0.05$; **: $p < 0.01$; ***: $p < 0.0005$; ****: $p < 0.0001$) All data presented as mean ± standard deviation

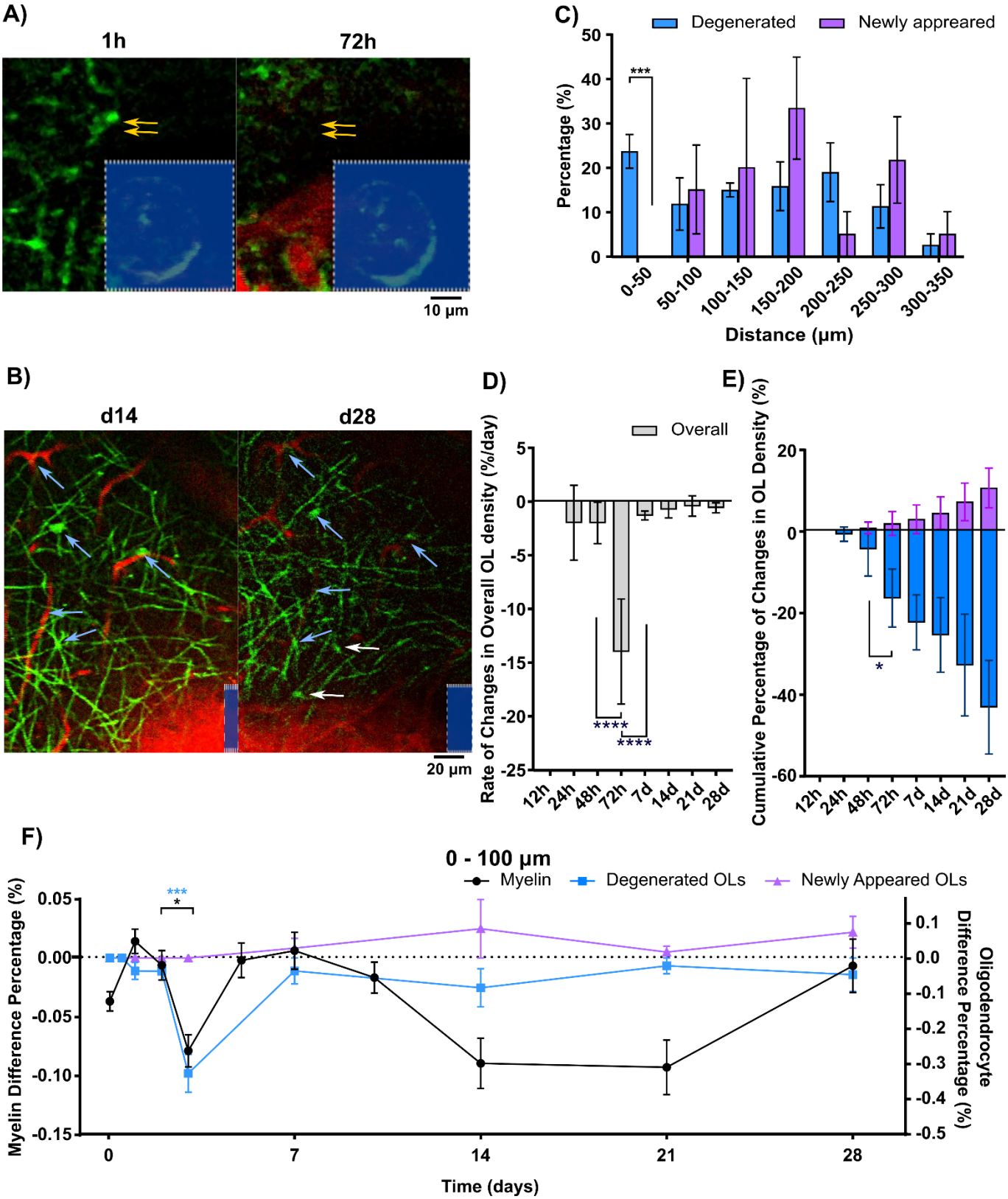

Figure 7. Oligodendrocyte degeneration and regeneration occur around chronic implant over 4 weeks. (**A**) Representative images of degeneration of a single oligodendrocyte near the implant at 72 h post-implantation. Red (sulforhodamine 101) indicates surrounding

blood vessels. (**B**) Oigodendrogenesis at tissue-electrode interface at 28 days following implantation. Blue arrows indicate the same oligodendrocytes and blood vessels as landmarks at 14 and 28 days, and white arrows show newly differentiated oligodendrocyte somas. (**C**) Histogram of degenerated/newly-differentiated oligodendrocytes over time as a function of distance (bins of 50 µm). Significant group-wise difference between the degenerated oligodendrocytes and oligodendrogenesis occurs at the first 50 µm radius bin ($p < 0.005$). (**D**) Changes in overall oligodendrocyte density over 250 µm away from the implant between consecutive time points (%/day). Degeneration of oligodendrocytes initiates at 24 h and reaches peak at 72 h post-implantation. (**E**) Changes in temporal patterns of cumulative density of degenerated/newly differentiated oligodendrocytes relative to 1 h control. Newly differentiated oligodendrocytes are observed starting at 48h post-implantation. (**F**) Time course relationship among myelin density, degenerated and newly differentiated oligodendrocytes within 100 µm from the implant. Both significant demyelination ($p < 0.05$) and oligodendrocyte degeneration ($p < 0.0005$) within 100 µm from the implant occurs between 48 h and 72 h post implantation. (*: $p < 0.05$; **: $p < 0.01$; ***: $p < 0.0005$; ****: $p < 0.0001$) All data except (**F**) are presented as mean ± standard deviation. Difference percentage is reported as mean ± standard error for clear visualization.

.

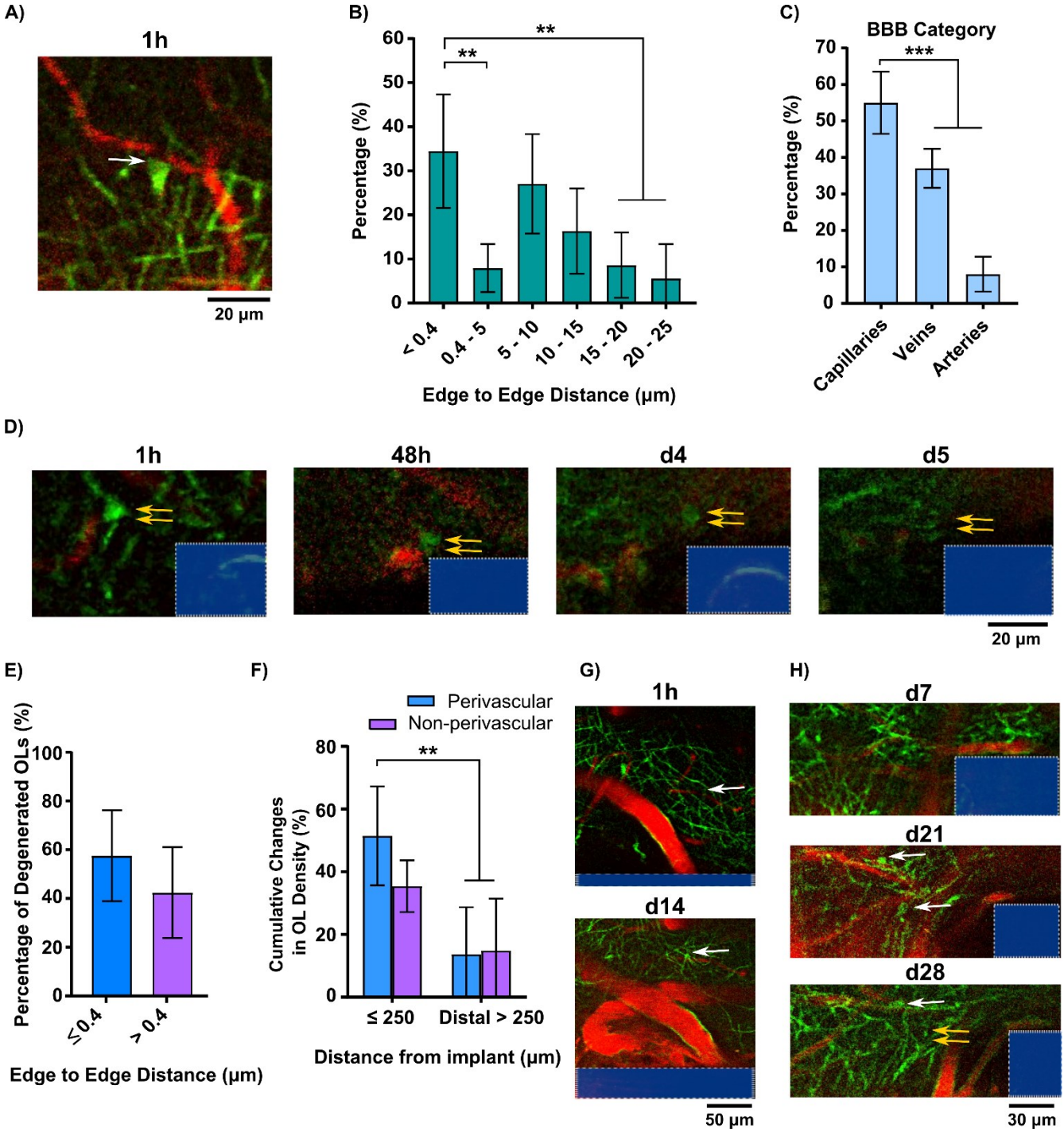

Figure 8. Perivascular oligodendrocytes on blood vessels are impaired by chronic implantation. (**A**) Representative images of a perivascular oligodendrocyte soma (green; white arrow) on surface of capillary blood vessel (red). (**B**) Distribution of oligodendrocyte

population as a function of distance between oligodendrocyte soma and blood vessel surface. (**C**) Types of blood vessels that have edge-to-edge distance less than minimal pixel resolution (≤ 0.4) with perivascular oligodendrocytes. (**D**) Time-series of perivascular oligodendrocyte degeneration near the implant (double yellow arrows indicate the perivascular oligodendrocyte eventually disappeared at d 5 post implantation). (**E**) Percent of degenerated oligodendrocytes over the perivascular subtype in edge-to-edge distance less than minimal pixel resolution and resting non-perivascular subtype (edge-to-edge distance > 0.4 μm) within the 250 μm away from the probe surface. (**F**) Percentage of oligodendrocyte subtypes that degenerated over time relative to 1 h post-insertion control in proximal (≤ 250 μm away from the implant) and distal regions (> 250 μm). (**G**) Regeneration of perivascular oligodendrocyte at tissue-electrode interface at day 14 post-implantation (white arrow). (**H**) Oligodendrogenesis at the tissue-electrode interface at day 21 post-implantation. One of these oligodendrocytes degenerates at 28 days post-implantation without remyelinating. (**: $p < 0.01$; ***: $p < 0.0005$) All data presented as mean ± standard deviation.

Data Availability

The raw/processed data required to reproduce these findings cannot be shared at this time as the data also forms part of an ongoing study.

References

[1] S.N. Flesher, J.L. Collinger, S.T. Foldes, J.M. Weiss, J.E. Downey, E.C. Tyler-Kabara, S.J. Bensmaia, A.B. Schwartz, M.L. Boninger, R.A. Gaunt, Intracortical microstimulation of human somatosensory cortex, Science Translational Medicine 8(361) (2016) 361ra141.

[2] J.E. Downey, L. Brane, R.A. Gaunt, E.C. Tyler-Kabara, M.L. Boninger, J.L. Collinger, Motor cortical activity changes during neuroprosthetic-controlled object interaction, Scientific Reports 7(1) (2017) 16947.

[3] K. Varghese, P. Molnar, M. Das, M.S. Kindy, B.C. Wheeler, J.J. Hickman, Microelectrode arrays and Alzheimer's disease: A novel in vitro investigative paradigm, Alzheimer's & Dementia: The Journal of the Alzheimer's Association 5(4) (2009) P428.

[4] H.G. Jahnke, A. Rothermel, I. Sternberger, T.G. Mack, R.G. Kurz, O. Panke, F. Striggow, A.A. Robitzki, An impedimetric microelectrode-based array sensor for label-free detection of tau hyperphosphorylation in human cells, Lab Chip 9(10) (2009) 1422-8.

[5] K.D. Foote, P. Seignourel, H.H. Fernandez, J. Romrell, E. Whidden, C. Jacobson, R.L. Rodriguez, M.S. Okun, Dual Electrode Thalamic Deep Brain Stimulation For The Treatment Of Posttraumatic And Multiple Sclerosis Tremor, Operative Neurosurgery 58(suppl_4) (2006) ONS-280-ONS-286.

[6] J. Volkmann, Deep Brain Stimulation for the Treatment of Parkinson's Disease, Journal of Clinical Neurophysiology 21(1) (2004).

[7] A.L. Benabid, S. Chabardes, J. Mitrofanis, P. Pollak, Deep brain stimulation of the subthalamic nucleus for the treatment of Parkinson's disease, The Lancet Neurology 8(1) (2009) 67-81.

[8] S. Little, A. Pogosyan, S. Neal, B. Zavala, L. Zrinzo, M. Hariz, T. Foltynie, P. Limousin, K. Ashkan, J. FitzGerald, A.L. Green, T.Z. Aziz, P. Brown, Adaptive deep brain stimulation in advanced Parkinson disease, Annals of Neurology 74(3) (2013) 449-457.

[9] X. Zhang, R.L. Zhang, Z.G. Zhang, M. Chopp, Measurement of neuronal activity of individual neurons after stroke in the rat using a microwire electrode array, Journal of Neuroscience Methods 162(1) (2007) 91-100.

[10] S.R. Soekadar, N. Birbaumer, L.G. Cohen, Brain–Computer Interfaces in the Rehabilitation of Stroke and Neurotrauma, in: K. Kansaku, L.G. Cohen (Eds.) Systems Neuroscience and Rehabilitation, Springer Japan, Tokyo, 2011, pp. 3-18.

[11] F. Quandt, F.C. Hummel, The influence of functional electrical stimulation on hand motor recovery in stroke patients: a review, Experimental & Translational Stroke Medicine 6(1) (2014) 9.

[12] J.L. Collinger, B. Wodlinger, J.E. Downey, W. Wang, E.C. Tyler-Kabara, D.J. Weber, A.J.C. McMorland, M. Velliste, M.L. Boninger, A.B. Schwartz, High-performance neuroprosthetic control by an individual with tetraplegia, The Lancet 381(9866) (2013) 557-564.

[13] P. Schucht, S. Moritz-Gasser, G. Herbet, A. Raabe, H. Duffau, Subcortical electrostimulation to identify network subserving motor control, Human Brain Mapping 34(11) (2013) 3023-3030.

[14] S.F. Lempka, M.D. Johnson, M.A. Moffitt, K.J. Otto, D.R. Kipke, C.C. McIntyre, Theoretical analysis of intracortical microelectrode recordings, Journal of Neural Engineering 8(4) (2011) 045006.

[15] J.C. Barrese, N. Rao, K. Paroo, C. Triebwasser, C. Vargas-Irwin, L. Franquemont, J.P. Donoghue, Failure mode analysis of silicon-based intracortical microelectrode arrays in non-human primates, Journal of neural engineering 10(6) (2013) 066014-066014.
[16] T.D.Y. Kozai, X. Li, L.M. Bodily, E.M. Caparosa, G.A. Zenonos, D.L. Carlisle, R.M. Friedlander, X.T. Cui, Effects of caspase-1 knockout on chronic neural recording quality and longevity: Insight into cellular and molecular mechanisms of the reactive tissue response, Biomaterials 35(36) (2014) 9620-9634.
[17] M. Jorfi, J.L. Skousen, C. Weder, J.R. Capadona, Progress towards biocompatible intracortical microelectrodes for neural interfacing applications, Journal of Neural Engineering 12(1) (2014) 011001.
[18] T. Saxena, L. Karumbaiah, E.A. Gaupp, R. Patkar, K. Patil, M. Betancur, G.B. Stanley, R.V. Bellamkonda, The impact of chronic blood–brain barrier breach on intracortical electrode function, Biomaterials 34(20) (2013) 4703-4713.
[19] G.C. McConnell, H.D. Rees, A.I. Levey, C.-A. Gutekunst, R.E. Gross, R.V. Bellamkonda, Implanted neural electrodes cause chronic, local inflammation that is correlated with local neurodegeneration, Journal of Neural Engineering 6(5) (2009) 056003.
[20] J.P. Seymour, D.R. Kipke, Neural probe design for reduced tissue encapsulation in CNS, Biomaterials 28(25) (2007) 3594-3607.
[21] T.D.Y. Kozai, N.B. Langhals, P.R. Patel, X. Deng, H. Zhang, K.L. Smith, J. Lahann, N.A. Kotov, D.R. Kipke, Ultrasmall implantable composite microelectrodes with bioactive surfaces for chronic neural interfaces, Nature Materials 11 (2012) 1065.
[22] E.S. Ereifej, G.M. Rial, J.K. Hermann, C.S. Smith, S.M. Meade, J.M. Rayyan, K. Chen, H. Feng, J.R. Capadona, Implantation of Neural Probes in the Brain Elicits Oxidative Stress, Frontiers in Bioengineering and Biotechnology 6 (2018) 9.
[23] S.M. Wellman, J.R. Eles, K.A. Ludwig, J.P. Seymour, N.J. Michelson, W.E. McFadden, A.L. Vazquez, T.D. Kozai, A Materials Roadmap to Functional Neural Interface Design, Advanced Functional Materials 28(12) (2018) 201701269.
[24] T.-i. Kim, J.G. McCall, Y.H. Jung, X. Huang, E.R. Siuda, Y. Li, J. Song, Y.M. Song, H.A. Pao, R.-H. Kim, C. Lu, S.D. Lee, I.-S. Song, G. Shin, R. Al-Hasani, S. Kim, M.P. Tan, Y. Huang, F.G. Omenetto, J.A. Rogers, M.R. Bruchas, Injectable, Cellular-Scale Optoelectronics with Applications for Wireless Optogenetics, Science 340(6129) (2013) 211.
[25] C.-H. Chen, C.-T. Lin, W.-L. Hsu, Y.-C. Chang, S.-R. Yeh, L.-J. Li, D.-J. Yao, A flexible hydrophilic-modified graphene microprobe for neural and cardiac recording, Nanomedicine: Nanotechnology, Biology and Medicine 9(5) (2013) 600-604.
[26] H. Zhang, P.R. Patel, Z. Xie, S.D. Swanson, X. Wang, N.A. Kotov, Tissue-Compliant Neural Implants from Microfabricated Carbon Nanotube Multilayer Composite, ACS Nano 7(9) (2013) 7619-7629.
[27] X. Cui, J. Wiler, M. Dzaman, R.A. Altschuler, D.C. Martin, In vivo studies of polypyrrole/peptide coated neural probes, Biomaterials 24(5) (2003) 777-787.
[28] J.K. Nguyen, M. Jorfi, K.L. Buchanan, D.J. Park, E.J. Foster, D.J. Tyler, S.J. Rowan, C. Weder, J.R. Capadona, Influence of resveratrol release on the tissue response to mechanically adaptive cortical implants, Acta Biomaterialia 29 (2016) 81-93.
[29] J.P. Seymour, F. Wu, K.D. Wise, E. Yoon, State-of-the-art MEMS and microsystem tools for brain research, Microsystems & Nanoengineering 3(1) (2017) 16066.
[30] S.M. Wellman, L. Li, Y. Yaxiaer, I. McNamara, T.D.Y. Kozai, Revealing Spatial and Temporal Patterns of Cell Death, Glial Proliferation, and Blood-Brain Barrier Dysfunction Around Implanted Intracortical Neural Interfaces, Frontiers in Neuroscience 13 (2019) 493.
[31] S.M. Wellman, T.D.Y. Kozai, In vivo spatiotemporal dynamics of NG2 glia activity caused by neural electrode implantation, Biomaterials 164 (2018) 121-133.
[32] L.A. Camuñas-Mesa, R.Q. Quiroga, A Detailed and Fast Model of Extracellular Recordings, Neural Computation 25(5) (2013) 1191-1212.

[33] V. Viswam, M.E.J. Obien, F. Franke, U. Frey, A. Hierlemann, Optimal Electrode Size for Multi-Scale Extracellular-Potential Recording From Neuronal Assemblies, Frontiers in neuroscience 13 (2019) 385-385.
[34] D.A. Henze, Z. Borhegyi, J. Csicsvari, A. Mamiya, K.D. Harris, G. Buzsaki, Intracellular features predicted by extracellular recordings in the hippocampus in vivo, J Neurophysiol 84(1) (2000) 390-400.
[35] N.J. Michelson, A.L. Vazquez, J.R. Eles, J.W. Salatino, E.K. Purcell, J.J. Williams, X.T. Cui, T.D.Y. Kozai, Multi-scale, multi-modal analysis uncovers complex relationship at the brain tissue-implant neural interface: new emphasis on the biological interface, J Neural Eng 15(3) (2018) 033001.
[36] C. Bennett, F. Mohammed, A. Álvarez-Ciara, M.A. Nguyen, W.D. Dietrich, S.M. Rajguru, W.J. Streit, A. Prasad, Neuroinflammation, oxidative stress, and blood-brain barrier (BBB) disruption in acute Utah electrode array implants and the effect of deferoxamine as an iron chelator on acute foreign body response, Biomaterials 188 (2019) 144-159.
[37] T.D.Y. Kozai, A.L. Vazquez, C.L. Weaver, S.-G. Kim, X.T. Cui, In vivotwo-photon microscopy reveals immediate microglial reaction to implantation of microelectrode through extension of processes, Journal of Neural Engineering 9(6) (2012) 066001.
[38] R. Biran, D.C. Martin, P.A. Tresco, Neuronal cell loss accompanies the brain tissue response to chronically implanted silicon microelectrode arrays, Experimental Neurology 195(1) (2005) 115-126.
[39] Y. Fan, L. Xie, C.Y. Chung, Signaling pathways controlling microglia chemotaxis, Molecules and Cells 40(3) (2017) 163-168.
[40] J.R. Eles, T.D.Y. Kozai, In vivo imaging of calcium and glutamate responses to intracortical microstimulation reveals distinct temporal responses of the neuropil and somatic compartments in layer II/III neurons, Biomaterials 234 (2020) 119767.
[41] S.M. Wellman, F. Cambi, T.D.Y. Kozai, The role of oligodendrocytes and their progenitors on neural interface technology: A novel perspective on tissue regeneration and repair, Biomaterials 183 (2018) 200-217.
[42] A. Nishiyama, M. Komitova, R. Suzuki, X. Zhu, Polydendrocytes (NG2 cells): multifunctional cells with lineage plasticity, Nature Reviews Neuroscience 10(1) (2009) 9-22.
[43] T. Kondo, M. Raff, Oligodendrocyte Precursor Cells Reprogrammed to Become Multipotential CNS Stem Cells, Science 289(5485) (2000) 1754.
[44] A.P. Sagare, R.D. Bell, Z. Zhao, Q. Ma, E.A. Winkler, A. Ramanathan, B.V. Zlokovic, Pericyte loss influences Alzheimer-like neurodegeneration in mice, Nature Communications 4(1) (2013) 2932.
[45] B.M. Morrison, Y. Lee, J.D. Rothstein, Oligodendroglia: metabolic supporters of axons, Trends in Cell Biology 23(12) (2013) 644-651.
[46] M.K. Desai, M.A. Mastrangelo, D.A. Ryan, K.L. Sudol, W.C. Narrow, W.J. Bowers, Early Oligodendrocyte/Myelin Pathology in Alzheimer's Disease Mice Constitutes a Novel Therapeutic Target, The American Journal of Pathology 177(3) (2010) 1422-1435.
[47] S.M. Wellman, K. Guzman, K.C. Stieger, L.E. Brink, S. Sridhar, M.T. Dubaniewicz, L. Li, F. Cambi, T.D.Y. Kozai, Cuprizone-induced oligodendrocyte loss and demyelination impairs recording performance of chronically implanted neural interfaces, Biomaterials 239 (2020) 119842.
[48] G.S. Tomassy, D.R. Berger, H.-H. Chen, N. Kasthuri, K.J. Hayworth, A. Vercelli, H.S. Seung, J.W. Lichtman, P. Arlotta, Distinct Profiles of Myelin Distribution Along Single Axons of Pyramidal Neurons in the Neocortex, Science 344(6181) (2014) 319.
[49] T. Philips, J.D. Rothstein, Oligodendroglia: metabolic supporters of neurons, J Clin Invest 127(9) (2017) 3271-3280.
[50] A. Almeida, J. Almeida, J.P. Bolaños, S. Moncada, Different responses of astrocytes and neurons to nitric oxide: The role of glycolytically generated ATP in astrocyte protection, Proceedings of the National Academy of Sciences 98(26) (2001) 15294.
[51] U. Fünfschilling, L.M. Supplie, D. Mahad, S. Boretius, A.S. Saab, J. Edgar, B.G. Brinkmann, C.M. Kassmann, I.D. Tzvetanova, W. Möbius, F. Diaz, D. Meijer, U. Suter, B. Hamprecht, M.W. Sereda, C.T. Moraes, J. Frahm, S. Goebbels, K.-A. Nave, Glycolytic oligodendrocytes maintain myelin and long-term axonal integrity, Nature 485 (2012) 517.

[52] Aiman S. Saab, Iva D. Tzvetavona, A. Trevisiol, S. Baltan, P. Dibaj, K. Kusch, W. Möbius, B. Goetze, Hannah M. Jahn, W. Huang, H. Steffens, Eike D. Schomburg, A. Pérez-Samartín, F. Pérez-Cerdá, D. Bakhtiari, C. Matute, S. Löwel, C. Griesinger, J. Hirrlinger, F. Kirchhoff, K.-A. Nave, Oligodendroglial NMDA Receptors Regulate Glucose Import and Axonal Energy Metabolism, Neuron 91(1) (2016) 119-132.
[53] A. Amaral, T. Meisingset, M. Kotter, U. Sonnewald, Metabolic Aspects of Neuron-Oligodendrocyte-Astrocyte Interactions, Frontiers in Endocrinology 4 (2013) 54.
[54] K.A. Kasischke, H.D. Vishwasrao, P.J. Fisher, W.R. Zipfel, W.W. Webb, Neural activity triggers neuronal oxidative metabolism followed by astrocytic glycolysis, Science 305(5680) (2004) 99-103.
[55] C. Howarth, P. Gleeson, D. Attwell, Updated energy budgets for neural computation in the neocortex and cerebellum, Journal of Cerebral Blood Flow & Metabolism 32(7) (2012) 1222-1232.
[56] M.K. Jha, B.M. Morrison, Glia-neuron energy metabolism in health and diseases: New insights into the role of nervous system metabolic transporters, Experimental neurology 309 (2018) 23-31.
[57] S.J. Won, B.H. Yoo, T.M. Kauppinen, B.Y. Choi, J.H. Kim, B.G. Jang, M.W. Lee, M. Sohn, J. Liu, R.A. Swanson, S.W. Suh, Recurrent/moderate hypoglycemia induces hippocampal dendritic injury, microglial activation, and cognitive impairment in diabetic rats, Journal of Neuroinflammation 9(1) (2012) 182.
[58] A.S. Saab, K.-A. Nave, A mechanism for myelin injury, Nature 529(7587) (2016) 474-475.
[59] I. Griffiths, M. Klugmann, T. Anderson, D. Yool, C. Thomson, M.H. Schwab, A. Schneider, F. Zimmermann, M. McCulloch, N. Nadon, K.-A. Nave, Axonal Swellings and Degeneration in Mice Lacking the Major Proteolipid of Myelin, Science 280(5369) (1998) 1610.
[60] M. Klugmann, M.H. Schwab, A. Pühlhofer, A. Schneider, F. Zimmermann, I.R. Griffiths, K.-A. Nave, Assembly of CNS Myelin in the Absence of Proteolipid Protein, Neuron 18(1) (1997) 59-70.
[61] C. Lappe-Siefke, S. Goebbels, M. Gravel, E. Nicksch, J. Lee, P.E. Braun, I.R. Griffiths, K.-A. Nave, Disruption of Cnp1 uncouples oligodendroglial functions in axonal support and myelination, Nature Genetics 33 (2003) 366.
[62] E.G. Hughes, J.L. Orthmann-Murphy, A.J. Langseth, D.E. Bergles, Myelin remodeling through experience-dependent oligodendrogenesis in the adult somatosensory cortex, Nature Neuroscience 21(5) (2018) 696-706.
[63] Y. Lee, B.M. Morrison, Y. Li, S. Lengacher, M.H. Farah, P.N. Hoffman, Y. Liu, A. Tsingalia, L. Jin, P.W. Zhang, L. Pellerin, P.J. Magistretti, J.D. Rothstein, Oligodendroglia metabolically support axons and contribute to neurodegeneration, Nature 487(7408) (2012) 443-8.
[64] I. Nikić, D. Merkler, C. Sorbara, M. Brinkoetter, M. Kreutzfeldt, F.M. Bareyre, W. Brück, D. Bishop, T. Misgeld, M. Kerschensteiner, A reversible form of axon damage in experimental autoimmune encephalomyelitis and multiple sclerosis, Nature Medicine 17(4) (2011) 495-499.
[65] P.G. Nijland, I. Michailidou, M.E. Witte, M.R. Mizee, S.M.A. van der Pol, B. van het Hof, A. Reijerkerk, L. Pellerin, P. van der Valk, H.E. de Vries, J. van Horssen, Cellular distribution of glucose and monocarboxylate transporters in human brain white matter and multiple sclerosis lesions, Glia 62(7) (2014) 1125-1141.
[66] K. Arai, E.H. Lo, Experimental models for analysis of oligodendrocyte pathophysiology in stroke, Experimental & Translational Stroke Medicine 1(1) (2009) 6.
[67] J.R. Eles, A.L. Vazquez, T.D.Y. Kozai, X.T. Cui, In vivo imaging of neuronal calcium during electrode implantation: Spatial and temporal mapping of damage and recovery, Biomaterials 174 (2018) 79-94.
[68] T.D.Y. Kozai, K. Catt, X. Li, Z.V. Gugel, V.T. Olafsson, A.L. Vazquez, X.T. Cui, Mechanical failure modes of chronically implanted planar silicon-based neural probes for laminar recording, Biomaterials 37 (2015) 25-39.
[69] Z.J. Du, C.L. Kolarcik, T.D.Y. Kozai, S.D. Luebben, S.A. Sapp, X.S. Zheng, J.A. Nabity, X.T. Cui, Ultrasoft microwire neural electrodes improve chronic tissue integration, Acta Biomaterialia 53 (2017) 46-58.
[70] Y. Deng, B. Kim, X. He, S. Kim, C. Lu, H. Wang, S.-G. Cho, Y. Hou, J. Li, X. Zhao, Q.R. Lu, Direct visualization of membrane architecture of myelinating cells in transgenic mice expressing membrane-anchored EGFP, Genesis 52(4) (2014) 341-349.
[71] Y. Wang, M. Ye, X. Kuang, Y. Li, S. Hu, A simplified morphological classification scheme for pyramidal cells in six layers of primary somatosensory cortex of juvenile rats, IBRO Rep 5 (2018) 74-90.

[72] M.C. LaPlaca, D.K. Cullen, J.J. McLoughlin, R.S. Cargill, High rate shear strain of three-dimensional neural cell cultures: a new in vitro traumatic brain injury model, Journal of Biomechanics 38(5) (2005) 1093-1105.
[73] E. Romanelli, D. Merkler, A. Mezydlo, M.-T. Weil, M.S. Weber, I. Nikić, S. Potz, E. Meinl, F.E.H. Matznick, M. Kreutzfeldt, A. Ghanem, K.-K. Conzelmann, I. Metz, W. Brück, M. Routh, M. Simons, D. Bishop, T. Misgeld, M. Kerschensteiner, Myelinosome formation represents an early stage of oligodendrocyte damage in multiple sclerosis and its animal model, Nature Communications 7 (2016) 13275.
[74] Q.-L. Cui, D. Khan, M. Rone, V. T.S. Rao, R.M. Johnson, Y.H. Lin, P.-A. Bilodeau, J.A. Hall, M. Rodriguez, T.E. Kennedy, S.K. Ludwin, J.P. Antel, Sublethal oligodendrocyte injury: A reversible condition in multiple sclerosis?, Annals of Neurology 81(6) (2017) 811-824.
[75] T.A. Evans, D.S. Barkauskas, J.T. Myers, E.G. Hare, J.Q. You, R.M. Ransohoff, A.Y. Huang, J. Silver, High-resolution intravital imaging reveals that blood-derived macrophages but not resident microglia facilitate secondary axonal dieback in traumatic spinal cord injury, Experimental Neurology 254 (2014) 109-120.
[76] T.A. Gennarelli, R. Tipperman, W.L. Maxwell, D.I. Graham, J.H. Adams, A. Irvine, Traumatic Damage to the Nodal Axolemma: an Early, Secondary Injury, in: A. Baethmann, O. Kempski, L. Schürer (Eds.) Mechanisms of Secondary Brain Damage, Springer Vienna, Vienna, 1993, pp. 49-52.
[77] B.D. Winslow, M.B. Christensen, W.-K. Yang, F. Solzbacher, P.A. Tresco, A comparison of the tissue response to chronically implanted Parylene-C-coated and uncoated planar silicon microelectrode arrays in rat cortex, Biomaterials 31(35) (2010) 9163-9172.
[78] B.D. Winslow, P.A. Tresco, Quantitative analysis of the tissue response to chronically implanted microwire electrodes in rat cortex, Biomaterials 31(7) (2010) 1558-1567.
[79] A.J. Woolley, H.A. Desai, K.J. Otto, Chronic intracortical microelectrode arrays induce non-uniform, depth-related tissue responses, Journal of neural engineering 10(2) (2013) 026007.
[80] V. Vostrikov, D. Orlovskaya, N. Uranova, Deficit of pericapillary oligodendrocytes in the prefrontal cortex in schizophrenia, The World Journal of Biological Psychiatry 9(1) (2008) 34-42.
[81] L.-D.D. Pham, K. Hayakawa, J.H. Seo, M.-N. Nguyen, A.T. Som, B.J. Lee, S. Guo, K.-W. Kim, E.H. Lo, K. Arai, Crosstalk between oligodendrocytes and cerebral endothelium contributes to vascular remodeling after white matter injury, Glia 60(6) (2012) 875-881.
[82] G. Buzsáki, Large-scale recording of neuronal ensembles, Nature Neuroscience 7(5) (2004) 446-451.
[83] C.S. Bjornsson, S.J. Oh, Y.A. Al-Kofahi, Y.J. Lim, K.L. Smith, J.N. Turner, S. De, B. Roysam, W. Shain, S.J. Kim, Effects of insertion conditions on tissue strain and vascular damage during neuroprosthetic device insertion, Journal of Neural Engineering 3(3) (2006) 196.
[84] M. Simons, T. Misgeld, M. Kerschensteiner, A unified cell biological perspective on axon-myelin injury, The Journal of cell biology 206(3) (2014) 335-345.
[85] N. Cao, Z.-X. Yao, Oligodendrocyte N-Methyl-d-aspartate Receptor Signaling: Insights into Its Functions, Molecular Neurobiology 47(2) (2013) 845-856.
[86] J.T. Neary, Protein kinase signaling cascades in CNS trauma, IUBMB Life 57(11) (2005) 711-718.
[87] S. Song, S. Wang, V.M. Pigott, T. Jiang, L.M. Foley, A. Mishra, R. Nayak, W. Zhu, G. Begum, Y. Shi, K.E. Carney, T.K. Hitchens, G.E. Shull, D. Sun, Selective role of Na(+) /H(+) exchanger in Cx3cr1(+) microglial activation, white matter demyelination, and post-stroke function recovery, Glia (2018).
[88] A. Campbell, C. Wu, Chronically Implanted Intracranial Electrodes: Tissue Reaction and Electrical Changes, Micromachines (Basel) 9(9) (2018) 430.
[89] Y. Tang, W. Le, Differential Roles of M1 and M2 Microglia in Neurodegenerative Diseases, Molecular Neurobiology 53(2) (2016) 1181-1194.
[90] G. Yiu, Z. He, Glial inhibition of CNS axon regeneration, Nat Rev Neurosci 7(8) (2006) 617-627.
[91] M. Sosa, H.R. Joo, L.M. Frank, Dorsal and Ventral Hippocampal Sharp-Wave Ripples Activate Distinct Nucleus Accumbens Networks, Neuron 105(4) (2020) 725-741. e8.
[92] R.J. Gardner, L. Lu, T. Wernle, M.-B. Moser, E.I. Moser, Correlation structure of grid cells is preserved during sleep, Nature neuroscience 22(4) (2019) 598-608.

[93] J. Krupic, M. Bauza, S. Burton, J. O'Keefe, Local transformations of the hippocampal cognitive map, Science 359(6380) (2018) 1143-1146.
[94] N. Miyamoto, L.-D.D. Pham, J.H. Seo, K.-W. Kim, E.H. Lo, K. Arai, Crosstalk between cerebral endothelium and oligodendrocyte, Cellular and Molecular Life Sciences 71(6) (2014) 1055-1066.
[95] F. Li, W.-C. Liu, Q. Wang, Y. Sun, H. Wang, X. Jin, NG2-glia cell proliferation and differentiation by glial growth factor 2 (GGF2), a strategy to promote functional recovery after ischemic stroke, Biochemical Pharmacology 171 (2020) 113720.
[96] C. Qin, W.-H. Fan, Q. Liu, K. Shang, M. Murugan, L.-J. Wu, W. Wang, D.-S. Tian, Fingolimod Protects Against Ischemic White Matter Damage by Modulating Microglia Toward M2 Polarization via STAT3 Pathway, Stroke 48(12) (2017) 3336-3346.
[97] J. McQueen, M.M. Reimer, P.R. Holland, Y. Manso, M. McLaughlin, J.H. Fowler, K. Horsburgh, Restoration of oligodendrocyte pools in a mouse model of chronic cerebral hypoperfusion, PloS one 9(2) (2014) e87227-e87227.
[98] N. Miyamoto, T. Maki, D. Pham Loc-Duyen, K. Hayakawa, H. Seo Ji, T. Mandeville Emiri, B. Mandeville Joseph, K.-W. Kim, H. Lo Eng, K. Arai, Oxidative Stress Interferes With White Matter Renewal After Prolonged Cerebral Hypoperfusion in Mice, Stroke 44(12) (2013) 3516-3521.
[99] J. Chen, S. Zuo, J. Wang, J. Huang, X. Zhang, Y. Liu, Y. Zhang, J. Zhao, J. Han, L. Xiong, M. Shi, Z. Liu, Aspirin promotes oligodendrocyte precursor cell proliferation and differentiation after white matter lesion, Front Aging Neurosci 6 (2014) 7-7.
[100] J. Liu, J.L. Dupree, M. Gacias, R. Frawley, T. Sikder, P. Naik, P. Casaccia, Clemastine Enhances Myelination in the Prefrontal Cortex and Rescues Behavioral Changes in Socially Isolated Mice, The Journal of Neuroscience 36(3) (2016) 957.
[101] S.T. Cooper, P.L. McNeil, Membrane Repair: Mechanisms and Pathophysiology, Physiol Rev 95(4) (2015) 1205-1240.
[102] G.Q. Bi, J.M. Alderton, R.A. Steinhardt, Calcium-regulated exocytosis is required for cell membrane resealing, The Journal of cell biology 131(6 Pt 2) (1995) 1747-1758.
[103] M. Caillaud, B. Chantemargue, L. Richard, L. Vignaud, F. Favreau, P.-A. Faye, P. Vignoles, F. Sturtz, P. Trouillas, J.-M. Vallat, A. Desmoulière, F. Billet, Local low dose curcumin treatment improves functional recovery and remyelination in a rat model of sciatic nerve crush through inhibition of oxidative stress, Neuropharmacology 139 (2018) 98-116.
[104] T. Shimizu, Y. Osanai, K.F. Tanaka, M. Abe, R. Natsume, K. Sakimura, K. Ikenaka, YAP functions as a mechanotransducer in oligodendrocyte morphogenesis and maturation, Glia 65(2) (2017) 360-374.
[105] T.D.Y. Kozai, A. Jaquins-Gerstl, A.L. Vazquez, A.C. Michael, X.T. Cui, Brain Tissue Responses to Neural Implants Impact Signal Sensitivity and Intervention Strategies, ACS Chemical Neuroscience 6(1) (2015) 48-67.
[106] I. Micu, Q. Jiang, E. Coderre, A. Ridsdale, L. Zhang, J. Woulfe, X. Yin, B.D. Trapp, J.E. McRory, R. Rehak, G.W. Zamponi, W. Wang, P.K. Stys, NMDA receptors mediate calcium accumulation in myelin during chemical ischaemia, Nature 439(7079) (2006) 988-992.
[107] M. Billger, M. Wallin, J.-O. Karlsson, Proteolysis of tubulin and microtubule-associated proteins 1 and 2 by calpain I and II. Difference in sensitivity of assembled and disassembled microtubules, Cell Calcium 9(1) (1988) 33-44.
[108] G.V.W. Johnson, J.M. Litersky, R.S. Jope, Degradation of Microtubule-Associated Protein 2 and Brain Spectrin by Calpain: A Comparative Study, Journal of Neurochemistry 56(5) (1991) 1630-1638.
[109] A. Kampfl, R. Posmantur, R. Nixon, F. Grynspan, X. Zhao, S.J. Liu, J.K. Newcomb, G.L. Clifton, R.L. Hayes, μ-Calpain Activation and Calpain-Mediated Cytoskeletal Proteolysis Following Traumatic Brain Injury, Journal of Neurochemistry 67(4) (1996) 1575-1583.
[110] C. Carvalho, P.I. Moreira, Oxidative Stress: A Major Player in Cerebrovascular Alterations Associated to Neurodegenerative Events, Front Physiol 9 (2018) 806-806.

[111] T. Hickey, D. Kreutzer, D.J. Burgess, F. Moussy, In vivo evaluation of a dexamethasone/PLGA microsphere system designed to suppress the inflammatory tissue response to implantable medical devices, Journal of Biomedical Materials Research 61(2) (2002) 180-187.
[112] O. Dechy-Cabaret, B. Martin-Vaca, D. Bourissou, Controlled Ring-Opening Polymerization of Lactide and Glycolide, Chemical Reviews 104(12) (2004) 6147-6176.
[113] Y. Zhong, R.V. Bellamkonda, Biomaterials for the central nervous system, J R Soc Interface 5(26) (2008) 957-975.
[114] U.A. Aregueta-Robles, A.J. Woolley, L.A. Poole-Warren, N.H. Lovell, R.A. Green, Organic electrode coatings for next-generation neural interfaces, Frontiers in neuroengineering 7 (2014) 15-15.
[115] M. Paukert, D.E. Bergles, Reduction of motion artifacts during in vivo two-photon imaging of brain through heartbeat triggered scanning, The Journal of physiology 590(13) (2012) 2955-2963.
[116] E.S. Ereifej, C.S. Smith, S.M. Meade, K. Chen, H. Feng, J.R. Capadona, The Neuroinflammatory Response to Nanopatterning Parallel Grooves into the Surface Structure of Intracortical Microelectrodes, Advanced Functional Materials 28(12) (2018) 1704420.
[117] J.P. Seymour, D.R. Kipke, Neural probe design for reduced tissue encapsulation in CNS, Biomaterials 28(25) (2007) 3594-607.